

**Department of Physics and Astronomy  
Ruprecht-Karls-Universität Heidelberg**

Bachelor Thesis in Physics  
submitted by

**Gregor Nicolas Ramien**

born in Bremen, Germany

**January 2017**



**GENERATION AND CONTROL OF X-RAY FREQUENCY  
COMBS THROUGH PERIODIC PHOTON  
MANIPULATION**

This Bachelor Thesis has been carried out by  
Gregor Nicolas Ramien  
at the  
Max Planck Institute for Nuclear Physics in Heidelberg  
under the supervision of  
Priv.-Doz. Dr. Adriana Pálffy

Gregor Nicolas Ramien: *Generation and Control of X-ray Frequency Combs through Periodic Photon Manipulation*, © January 2017

# ABSTRACT

---

## *English*

The possibility to generate and control x-ray frequency combs via periodic manipulation of the hyperfine magnetic field  $B$  in a nuclear forward scattering (NFS) setup is investigated theoretically. We consider NFS of x-ray pulses off a thin sample containing  $^{57}\text{Fe}$  Mößbauer nuclei. These nuclei present a very narrow-band resonance at 14.4 keV. The magnetic field manipulation relies on periodic sequences of switching off and back on the B-field, which corresponds to coherent storage of the x-ray photon, and phase modulation by employing rotations by  $180^\circ$  of the B-field direction. Our numerical results show that x-ray combs with very narrow, equidistant peaks around the nuclear resonance energy can be generated and manipulated by tuning the parameters of the magnetic field switching sequence. Possible applications for metrology and quantum technology are anticipated.

## *Deutsch*

Die Möglichkeit der Erzeugung und Kontrolle von Röntgen-Frequenzkämmen durch die Manipulation eines hyperfeinen magnetischen Feldes  $B$  in einem auf Kernresonanzstreuung in Vorwärtsrichtung (NFS) basierendem Aufbau wird theoretisch untersucht. Wir betrachten Röntgenpulse, die im Rahmen von NFS an einer dünnen Probe mit  $^{57}\text{Fe}$  Mößbauer-Kernen streuen. Diese Kerne haben eine sehr schmale Resonanz bei 14.4 keV. Die magnetischen Schaltsequenzen basieren zum einen auf einem Aus- und wieder Anschalten des B-Feldes, wodurch eine kohärente Speicherung des Röntgenphotons induziert wird. Zum anderen verwenden die Sequenzen eine Rotation der Magnetfeldrichtung um  $180^\circ$ , welche zu einer Phasenmodulation des Photons führt. Unsere numerischen Resultate zeigen: Es ist möglich, sehr schmale, äquidistante Peaks nahe der Kernresonanzenergie zu generieren und zu manipulieren, indem man die Parameter der magnetischen Schaltsequenzen verändert. Mögliche Anwendungen werden in der Messtechnik und Quantentechnologie gesehen.



*"Life is like riding a bicycle. To keep your balance, you must keep moving."*

— Albert Einstein

## ACKNOWLEDGEMENTS

---

First of all, I would like to thank PD Dr. Adriana Pálffy for her thorough and very diligent supervision. It is due to her great expertise and careful attention to detail, that my thesis could fulfil the requirements of a current scientific work. Thank you for providing a highly intriguing topic, the prospect of Quantum Computing really fuelled my enthusiasm throughout this whole project. I am also genuinely grateful for your prudence and patience with proof-reading my work short before the deadline.

Second, I would like to emphasize my appreciation for the strong and profound support of Dr. Jonas Gunst. Thank you for always alleviating my concerns with the topic and for providing helpful and motivating assistance. The discussions with you were always very pleasant and productive.

In this context, thanks also go to Dr. Xiangjin Kong, who contributed to the ideas of this project.

Furthermore, I would like to thank Prof. Dr. Christoph Keitel for allowing me to join his group at the Max Planck Institute and for providing me with work resources. Thanks to the whole group for the nice atmosphere in the office and a great Christmas party.

Finally, let me thank my family, especially my mother Marion Ramien, for great moral support and encouragement.





# CONTENTS

---

<b>I</b>	<b>PREPARATIONS</b>	<b>1</b>
1	INTRODUCTION	3
1.1	Motivation . . . . .	3
1.2	Nuclear Forward Scattering . . . . .	6
2	THEORETICAL MODEL	13
2.1	Master Equation . . . . .	14
2.2	The Hamiltonian . . . . .	16
2.3	Optical Bloch Equations . . . . .	17
2.4	The Matrix Elements . . . . .	20
2.5	The Wave Equation . . . . .	24
2.6	Decoherence Matrix . . . . .	27
2.7	Maxwell-Bloch Equations . . . . .	29
<b>II</b>	<b>NUMERICAL RESULTS</b>	<b>31</b>
3	COHERENT PHOTON STORAGE AND PHASE MODULATION	33
3.1	Resonantly Scattered Field Amplitude . . . . .	33
3.2	Storage Effect . . . . .	37
3.3	Phase Modulation . . . . .	38
4	GENERATION AND CONTROL OF FREQUENCY COMBS	41
4.1	Fourier Transform . . . . .	42
4.2	Qualitative Analysis . . . . .	44
4.3	Analytic Approach . . . . .	47
4.4	Feasibility . . . . .	52
5	SUMMARY AND OUTLOOK	57
<b>III</b>	<b>APPENDIX</b>	<b>61</b>
A	APPENDIX A	63
	BIBLIOGRAPHY	65

## ACRONYMS

---

NFS Nuclear Forward Scattering

QB Quantum Beat

QM Quantum Mechanics

qm quantum mechanical

MBE Maxwell-Bloch Equations

OBE Optical Bloch Equations

SVE slowly varying envelope

Inv inverting sequence

NInv non-inverting sequence

PDE partial differential equation

## Part I

### PREPARATIONS

This part contains the general introduction and the derivation of the theoretical model employed. It initially provides a rough overview of this thesis' contents and subsequently explains the frame we work in.



# INTRODUCTION

---

## 1.1 MOTIVATION

One of the key players for the development of quantum technologies is the photon as a flying qubit. It has the potential to become the fastest information carrier of tomorrow [1]. Present applications employ infrared, microwave and optical photons for photonic devices such as quantum photonic circuits [2] and quantum memories [3, 4]. However, from the angle of miniaturization, the large wavelengths of these photons and their corresponding diffraction limit pose a bottleneck to the predictions of Moore's Law [5]. Moving to shorter wavelengths, e.g. x-ray photons, would drastically reduce the limitation on the spatial dimensions. Apart from the smaller diffraction limit, x-rays convince with their deep penetration power, robustness and spatial resolution which potentially reaches down to atomic scales.

In addition, prospects for possible applications in quantum information and quantum optics [6] are fuelled by the recent commissioning of coherent x-ray sources [7, 8], new optical elements in this wavelength regime [9, 10] and nearly lossless detection efficiencies.

In order to employ the x-ray photons as qubits, it is inevitable to be able to control their core properties. As the x-ray wavelengths range on the energy scale of inner-shell atomic transitions [11] and low-lying nuclear transitions [12, 13], the resonant interaction might be exploited to exert control on the photons. First experiments in this topic have investigated non-linear effects of x-rays interacting with atoms [14, 15] as well as collective phenomena in the resonant scattering off nuclei [12, 16, 17]. The advantages of using nuclear transitions include that nuclei are clean, well-isolated systems that provide long coherence times and can be found in high-density solid-state targets.

One of the photon properties sought to control is their propagation speed. Even if just on a timescale of several hundred nanoseconds, the temporal qubit

storage is a key tool.

As was shown pioneeringly in Ref. [18] in 1996, storage of the photonic energy may be achieved in a Nuclear Forward Scattering (NFS) setup (see section 1.2) using nuclear resonances. The principal effect in NFS is the temporal creation of a delocalized nuclei excitation (Nuclear Exciton). At resonance, instead of exciting one single particular nucleus, the photon generates a collective excitation, that decays coherently in the forward direction [19].

Since 1996, theoretical research into this topic revealed further control opportunities through the manipulation of the external magnetic field. E.g. in Ref. [20], it was recently proposed that the rotation of the field can be used as a control knob to perform logical operations with the polarization of the flying qubits. Additionally, in Ref. [1], a fully coherent storage conserving not just energy but also phase and polarization of the photon was presented along with a  $180^\circ$  photon phase modulation. Here, the storage is achieved by switching off a previously present magnetic field embedding the nuclei. Switching the field back on at a later time releases the photon again. Furthermore, a shift of  $180^\circ$  in the scattered photon phase can be induced by abruptly rotating the field by  $180^\circ$ , so that the quantization axis is inverted. Moreover, it turns out that storage could be even more robust and more flexible when using special layered structures that contain a nanometer-thick iron film [21].

It is within the framework of the two mechanisms of storage and phase modulation where the findings of this thesis originate. We exploit the fact that these mechanisms can be combined and applied repetitively in a switching sequence. Instead of sticking to one single storage process, we theoretically investigate the effects of performing storage and modulation in a periodic pattern.

To do so, we choose a specific NFS geometry (see fig. 2), in which a short x-ray pulse of 1 ns duration shines onto a  $^{57}\text{Fe}$  Mößbauer target.

Two main types of periodic magnetic switching sequences are tested with a field strength of  $B_0 = 34.4$  T:

- i) The magnetic field alternates between 0 and  $B_0$ , while its direction is not altered. We refer to this as the "non-inverting" sequence in the following.
- ii) The direction of the field is rotated by  $180^\circ$  so that it alternates between  $-B_0$ , 0 and  $B_0$ . We subsequently label this sequence "inverting".

Since we expect the periodicity to have an impact on the frequency composition of the forward detected radiation, we monitor the frequency as well as the time spectrum response.

Our numerical simulations show: comb structures of equidistant peaks emerge in the frequency domain of the resonantly forward scattered x-ray radiation.

Depending on the specific parameters of the switching series, the combs change their shape. The increasing of the storage time narrows the combs and manifold the frequency peaks, while the overall intensity declines. The combs of the non-inverting and the inverting series are shifted against each other by half their equidistant separation.

The generation of these frequency combs bears two opportunities. Firstly, the obvious utility is the application as a measurement instrument in the usual sense of frequency combs. In particular, the peak width in the order of tens of neV suggests actual opportunities. Secondly, since the distinctive form of the combs can be controlled via the parameters of the magnetic switching, a utilization to encode information is imaginable!

This work is structured as follows. In the remaining section of this chapter, we give a brief introduction to the physical base supporting this thesis, the NFS mechanism. We present the concept of Nuclear Exciton and describe the experimental setup theoretically considered. In the subsequent chapter 2, we lay the groundwork to theoretically investigate the dynamics of a light pulse propagating through a resonant medium. We start from a general Hamiltonian that can be split into an unperturbed and a perturbed part. We proceed by choosing a semi-classical approach to describe the radiation-nucleus interaction and by specifying a four-level quantum system. We close by putting forward the Maxwell-Bloch Equations (MBE) specific to our ansatz.

As the two photon manipulation techniques presented in Ref. [1] play a central role in our investigation methods, we dedicate chapter 3 to the reproduction of these results. We also provide a detailed description of the observed time spectra.

The likely most important chapter is chapter 4. There, we put forward the numerical results of investigating the scattered light dynamics under the influence of a periodically changing external magnetic field. We investigate the

generation and behaviour of above mentioned frequency combs and discuss their experimental practicability.

Finally, we draw conclusions from our results and present an outlook for the generation and use of the x-ray frequency combs.

## 1.2 NUCLEAR FORWARD SCATTERING

The foundation of our whole model is the phenomenon of Nuclear Forward Scattering (NFS). It is characterized by two main traits:

- the scattering happens in the same direction as the incident light (forward),
- collective effects (superradiance) occur.

The centrepiece of NFS is the Mößbauer effect.

The German physicist Rudolf Mößbauer originally set out to investigate the probability of reabsorption of  $\gamma$ -rays within solid-state samples. In 1958, he unexpectedly made an impactful discovery: the recoilless nuclear absorption of  $\gamma$ -ray photons.

Consider a  $\gamma$ -photon impinging on a target of absorbent particles, e.g. nuclei. The photon's energy has to cover the natural transition energy  $\hbar\omega_t$  within a deviation of the natural linewidth  $\Gamma$ . Additionally, it has to provide the energy lost in recoil  $E_{rec}$  in order to drive an excitation:  $E_\gamma \stackrel{!}{=} \hbar\omega_t + E_{rec}$ .

If we have a homogeneous crystal target, all nuclei require the same energy to be excited. Hence, for a sufficiently small linewidth, a re-absorption within the medium can only occur if the photon or nucleus initially and after first re-emission compensates  $E_{rec}$  with energy additional to  $E_\gamma$ .

Multiple resonant scattering would therefore be possible in case the movement of the nuclei, i.e. phonon oscillations, provided such energy. Or if the recoil was negligible with respect to the transition width.

As Mößbauer revealed for specific materials, in re-absorption effects not involving phonons, for some scattering processes  $E_{rec}$  is sufficiently small due to a distributive nature of the excitation: the photon recoil collectively and equally spreads among all nuclei bound in the crystal. With the crystal mass



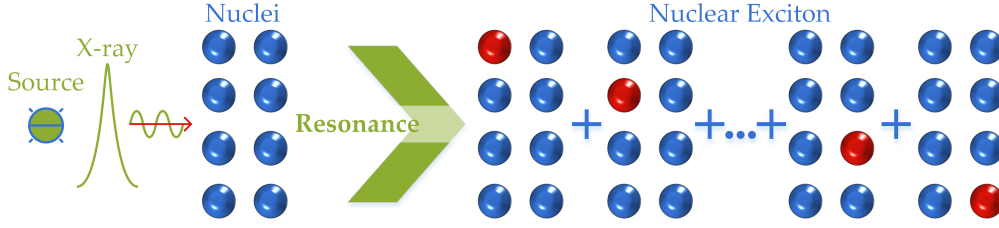


Figure 1: Schematic sketch of the Nuclear Exciton generation. A resonant light pulse (green) impinges on a crystal target (blue). The resulting excitation is delocalized and can therefore be described as a superposition of all possible single excitations (red).

being a macroscopic quantity, the recoil energy becomes negligible.

Starting from momentum conservation  $|p_{\text{rec}}| \stackrel{!}{=} |p_{\gamma}|$ , i.e.

$$\frac{E_{\gamma}}{c} = p_{\gamma} \stackrel{!}{=} p_{\text{rec}} = \sqrt{2ME_{\text{rec}}}, \quad (1.1)$$

we find for the recoil energy:

$$E_{\text{rec}} = \frac{E_{\gamma}^2}{2Mc^2}, \quad (1.2)$$

with the mass  $M$  of the collision partner.

The most popular Mößbauer nucleus is  $^{57}\text{Fe}$  which has a mass of  $m = 5.3 \cdot 10^{-7} \text{ keV}/c^2$  and  $E_{\gamma} = E_{\text{t}} = 14.4 \text{ keV}$  for the transition from the ground to the first excited state. We can find the natural linewidth  $\Gamma = 2\Delta E$  from the uncertainty principle  $\Delta E \Delta t \geq \hbar/2$  when setting the time imprecision to be the excited state's lifetime  $\tau$ , which is  $\tau = 141 \text{ ns}$  in the case of  $^{57}\text{Fe}$ .

Herewith, the recoil/linewidth energy ratio is

$$\frac{E_{\text{rec}}}{\Gamma} = \frac{E_{\gamma}^2 \tau}{2M\hbar c^2} = \frac{1}{N} \frac{E_{\gamma}^2 \tau}{2m\hbar c^2} \approx \frac{4.3 \cdot 10^5}{N}, \quad (1.3)$$

with  $M = N \cdot m$  as the mass of the crystal consisting of  $N$  single iron nuclei. We can see that for the Avogadro number  $\frac{E_{\text{rec}}}{\Gamma} \approx 10^{-18}$  and for  $N \rightarrow \infty$ , the ratio converges to zero.

The recoilless absorption has a number of interesting and useful properties for the forward directed emission, i.e. photons scattered in their incidence direction:

- The lattice nuclei are kicked in a collective fashion. If additionally no

spin flip or other conversion occurs, there is no way of telling from the forward scattered radiation, which single nucleus was excited by the photon. The excitation is delocalized and it may be described as a superposition of all single nuclei. This is referred to as the "Nuclear Exciton" or "Timed Dicke State" in literature [22]. We may write its state as [23]

$$|\Psi_{NE}\rangle = \frac{1}{\sqrt{N}} \sum_{l=1}^N e^{ik_0 r_l} |g_{\setminus l}\rangle |e_l\rangle$$

with  $|g_{\setminus l}\rangle |e_l\rangle$  symbolizing a state in which the  $l$ -th nucleus at position  $r_l$  is excited (denoted by  $|e_l\rangle$ ) while all other but  $l$  stay in the ground state ( $|g_{\setminus l}\rangle$ ). The wave vector of the incident photon is labelled  $\mathbf{k}_0$ .

- Distinguishability in the time spectrum: Other scattering effects like Compton scattering or photoelectric effects are prompt, but the absorption-emission scattering of NFS is delayed by several nanoseconds [24]. The NFS response can therefore be distinguished simply by viewing the time spectrum from a certain delay point.
- Multiple scattering effects: For a large number of nuclei, the photon is resonantly and coherently scattered several times before leaving the target. The superposition of these excitations creates oscillations in the detected intensity (see chapter 3).

### Setup

In our model (see chapter 2), we consider a  $^{57}\text{Fe}$  solid-state sample. It is immersed in a magnetic field, determining the quantization axis to be  $y$  as shown in figure 2.

The target is penetrated by a short x-ray pulse (e.g. from a last generation synchrotron radiation or x-ray free electron laser (XFEL) [25] source) propagating in  $z$ -direction. We tune the laser to drive the  $M_1$ -transition of the Mößbauer nuclei between ground  $|g\rangle$  and first excited state  $|e\rangle$ , which is at  $\hbar\omega_0 = 14.4$  keV. The nuclear spins are  $I_g = 1/2$  and  $I_e = 3/2$ , allowing for a degeneracy via the magnetic quantum numbers  $M_g = \pm 1/2$ ,  $M_e = -3/2, \dots, 3/2$ . During periods when the magnetic field is present, the field lifts the degeneracy by separating the levels by their Zeeman splitting  $\Delta_g$ ,  $\Delta_e$  for ground and excited state

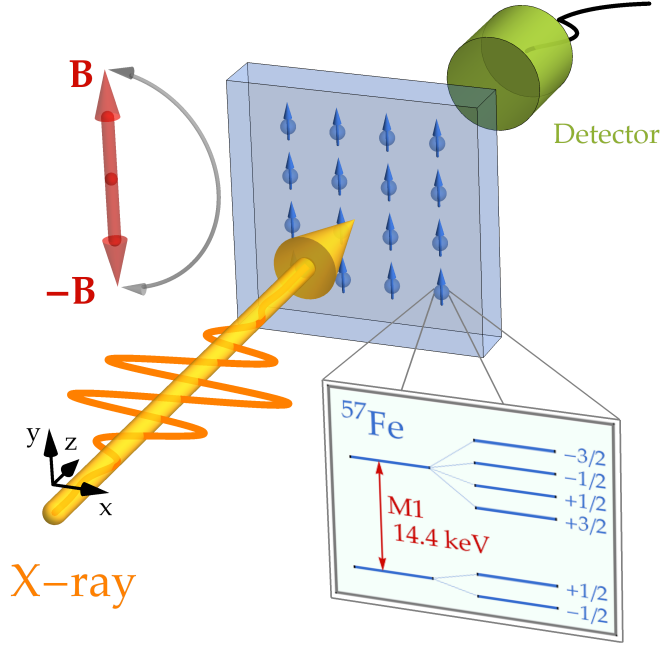


Figure 2: This figure shows the Nuclear Forward Scattering setup. The x-ray (orange) propagating along the  $z$ -direction penetrates the Mössbauer target. The probe experiences a magnetic field  $B$ , that can be switched off, on and rotated by  $\pi$  rad, so that the quantization axis is inverted. The inset shows the level scheme of the ground  $g$  and first excited  $e$  state of the  $^{57}\text{Fe}$  sample including magnetic degeneracy. The two states have the nuclear spins  $I_g = 1/2$ ,  $I_e = -1/2$ , with magnetic quantum number degeneracies  $M_g \in \{-1/2, 1/2\}$  and  $M_e \in \{-3/2, -1/2, 1/2, 3/2\}$  as shown in the inset. Many thanks to Jonas Gunst [27] for providing the image basis.

respectively. Since the pulse is wider than these splittings, it simultaneously addresses all possible six transitions which fulfil  $\Delta M := M_e - M_g \in \{-1, 0, 1\}$ . Following the steps in Ref. [26], we can find a way of describing the dependence of the scattered field amplitude on the setup geometry.

The coherently forward scattered radiation amplitude  $E(z, t)$  can be determined from the iteratively solvable wave equation [28, 29]

$$\partial_z E(z, t) = - \sum_l K_l \mathbf{J}_l(t) \int_{-\infty}^t \mathbf{J}_l^\dagger(\tau) E(z, \tau) d\tau, \quad (1.4)$$

with a constant  $K_l$ . The summation index  $l$  runs over all combinations of  $M_g$ ,  $M_e$  for each nuclear site in the sample.

The nuclear transition current matrix elements  $\mathbf{J}_l(t) = \langle I_g M_g | \mathbf{J}(t) | I_e M_e \rangle$  and  $\mathbf{J}_l^\dagger$  represent excitation and de-excitation processes in the resonant scattering. The  $\mathbf{J}$  operators are time-dependently proportional to the nuclear current den-

sity operator in momentum representation  $\mathbf{j}(\mathbf{k})$ , so that we can write

$$\mathbf{J}_l^\dagger(t) \sim \langle I_g M_g | \mathbf{j}^\dagger(\mathbf{k}) | I_e M_e \rangle = \mathbf{j}_l^\dagger(\mathbf{k}). \quad (1.5)$$

These density matrix elements are given for M1 transitions by [28, 30]

$$\mathbf{j}_l^\dagger(\mathbf{k}) = \sqrt{\frac{3(2I_e + 1)c^5\Gamma_\gamma}{4\omega_0^3}} \sum_{q=0,\pm 1} \begin{pmatrix} I_g & 1 & I_e \\ -M_g & q & M_e \end{pmatrix} (-1)^q \mathbf{k} \times \mathbf{n}_{-q}^*, \quad (1.6)$$

with the matrix denoting the Wigner 3-j symbol and the wave vector  $\mathbf{k}$  of the incident light. We denote the speed of light by  $c$ , the M1-transition frequency by  $\omega_0$  and the radiative decay rate of the excited state by  $\Gamma_\gamma$ .

The  $\mathbf{n}_q$  are spherical unit vectors that depend on the dictation of the quantization axis via the magnetic field. In Cartesian coordinates (with the canonical basis vectors  $\mathbf{e}_i$ ), they are given by

$$\begin{aligned} \mathbf{n}_0 &= \mathbf{e}_y, \\ \mathbf{n}_{+1} &= -\frac{1}{\sqrt{2}}(\mathbf{e}_x + i\mathbf{e}_z), \\ \mathbf{n}_{-1} &= \frac{1}{\sqrt{2}}(\mathbf{e}_x - i\mathbf{e}_z). \end{aligned} \quad (1.7)$$

The vectorial orientation of the scattered field amplitude is given by its polarization  $\mathbf{e}_0$ , so that  $\mathbf{E}_0(z, t) \sim \mathbf{e}_0$ . Going back to Eq. (1.4), we see that the scattered amplitude for a single nuclear site and single  $l = (M_g, M_e)$  is proportional to the scalar product

$$\begin{aligned} \mathbf{J}_l^\dagger(t)E(z, t) &\sim \mathbf{j}_l^\dagger(\mathbf{k})\mathbf{e}_0 \\ &\sim \mathbf{e}_0 \left( \sum_{q=0,\pm 1} \begin{pmatrix} I_g & 1 & I_e \\ -M_g & q & M_e \end{pmatrix} (-1)^q \mathbf{k} \times \mathbf{n}_{-q}^* \right) \\ &\stackrel{*}{=} \mathbf{e}_0 \left( \begin{pmatrix} I_g & 1 & I_e \\ -M_g & (M_g - M_e) & M_e \end{pmatrix} (-1)^{(M_g - M_e)} \mathbf{k} \times \mathbf{n}_{(M_e - M_g)}^* \right), \end{aligned} \quad (1.8)$$

where in (\*) we have used that the index  $q$  is determined by the 3-j symbol properties which demand  $q = M_g - M_e$  in order for the symbol to not be zero [31]. Therefore  $-q$  is equal to  $\Delta M$  from above.

This last term in Eq. (1.8) vanishes for certain combinations of the polarization, wave vector and quantization axis orientations. This means that for specific geometries, some pairs  $(M_g, M_e)$  do not contribute to the scattered field amplitude and the six level system's output is effectively reduced to a fewer level system's output.

To constrain our system in the inset in figure 2 to only four levels (see figure 3 on page 17), we set the x-ray pulse to be linearly polarized along the  $x$ -axis (so that  $\mathbf{e}_0 = \mathbf{e}_x$ ). In combination with the displayed B-field geometry, the selection rule  $\Delta M = 0$  kicks in [26]. Our four level system then consists of the  $M_g = \pm 1/2$  and  $M_e = \pm 1/2$  levels since only the two  $\Delta M = 0$  transitions are driven by the laser.



## THEORETICAL MODEL

---

In this chapter we derive the fundamental equations used in this thesis to describe the dynamic of a light pulse propagating through a target with resonant nuclei.

Our approach is based on a semi-classical description: while we treat the nuclei fully quantized, we approximate the radiation classically. This ansatz, despite eventually appearing controversial on first sight, has proven to agree very well with experimental results [18, 32–34].

Starting from the Schrödinger equation, we employ the density matrix formalism to describe our system via the Master Equation. The Master Equation provides us with the Optical Bloch Equations (OBE). Linking the interaction Hamiltonian to reduced transition probabilities  $\mathcal{B}$ , permits us to relate the OBE to the wave equation of the light beam. We thereby arrive at our final set of equations, the Maxwell-Bloch Equations (MBE). These coupled partial differential equations can then be solved numerically.

Since we later on investigate the case of linearly polarized light incident on  $^{57}\text{Fe}$  Mößbauer nuclei (see fig. 2 on page 9), we can always find a B-field geometry where only the  $\Delta M = 0$  transitions are driven. In this geometry the description of the light-nucleus interaction can be simplified to a four-level system as shown in figure 3.

In the following, we derive the MBE for such a system.

## 2.1 MASTER EQUATION

*Pure and Mixed States*

In Quantum Mechanics (QM), the evolution of a state  $|\psi\rangle$  of a system is governed by the Schrödinger equation [35]

$$i\hbar\partial_t |\psi\rangle = \hat{H} |\psi\rangle, \quad (2.1)$$

where the states  $|\psi\rangle$  are elements of a Hilbert space  $H$ .

If it is possible to express  $|\psi\rangle$  as a linear combination of an eigenstate basis  $B := \{|\phi_i\rangle\}_i$  of  $H$ , then  $|\psi\rangle$  is called a pure state, i.e.

$$|\psi\rangle = \sum_i \alpha_i |\phi_i\rangle. \quad (2.2)$$

The expansion coefficients are given by the projection of the state onto the respective basis element,  $\alpha_i = \langle \phi_i | \psi \rangle$ . They represent the probability amplitudes of finding the eigenvalue of  $|\phi_i\rangle$  when collapsing the wave function in a measurement [35].

This probability  $p_{QM} = \|\alpha_i\|^2$  does not represent a classical probability in the mathematical sense. Meaning that, before the measurement, the pure state  $|\psi\rangle$  is not in just one eigenstate with a certain likeliness, but in a quantum mechanical superposition of all eigenstates at the same time.

Now, let us consider an ensemble of pure states  $|\psi_i\rangle$ , which may be from different Hilbert spaces. If we let the ensemble (independent from measurement) be in just one of those states with a certain likeliness  $p_i$  at the same time, we have a classical statistical ensemble with classical probabilities  $p_i$ .

The difference between  $p_i$  and  $p_{QM}$  is that the first one is based on uncertainty, i.e. a simple lack of information available to the observer, while the latter represents the genuine, counter-intuitive indetermination of qm objects.



### Density Matrix Formalism

To describe such a statistical ensemble, also referred to as a mixed state, we may introduce the density matrix formalism [35]:

$$\hat{\rho} : H_1 \otimes H_2 \otimes \dots \otimes H_m \rightarrow H_i, |\Phi\rangle \mapsto \hat{\rho}|\Phi\rangle, \quad (2.3)$$

where  $\otimes$  denotes the tensor product,  $\hat{\rho}$  is the density matrix itself and  $H_n$  are Hilbert spaces.

Making the definition

$$\hat{\rho} := \sum_i p_i |\psi_i\rangle \langle \psi_i|, \quad (2.4)$$

we can find the time evolution of our statistical ensemble from (2.1):

$$\begin{aligned} \partial_t \hat{\rho} &= \partial_t \sum_i p_i |\psi_i\rangle \langle \psi_i| = \sum_i p_i (\partial_t |\psi_i\rangle \langle \psi_i| + |\psi_i\rangle \partial_t \langle \psi_i|) \\ &= \frac{-i}{\hbar} \sum_i p_i (\hat{H} |\psi_i\rangle \langle \psi_i| + |\psi_i\rangle \hat{H} \langle \psi_i|) \\ &= \frac{-i}{\hbar} \sum_i p_i [\hat{H}, |\psi_i\rangle \langle \psi_i|] = \frac{-i}{\hbar} [\hat{H}, \hat{\rho}] \\ &\implies \partial_t \hat{\rho} = \frac{1}{i\hbar} [\hat{H}, \hat{\rho}]. \end{aligned} \quad (2.5)$$

With (2.5), which is also known as the von Neumann equation, we have found a way of telling the state of our system  $\hat{\rho}(t)$  at given times  $t$ .

The diagonal matrix elements  $\langle \psi_i | \hat{\rho} | \psi_i \rangle =: \rho_{ii}$  are called populations for they describe the populations of the state  $|\psi_i\rangle$ , while the off-diagonals  $\rho_{ij}, i \neq j$ , are referred to as coherences since they give a measure of the coherence between  $|\psi_i\rangle$  and  $|\psi_j\rangle$ .

So far, we have not specified the Hamiltonian of the system we are describing. In principal, Eq. (2.5) is qualified to fully describe the systems time evolution. However, its scope depends on the given Hamiltonian. It is possible, for example in the case of taking a semi-classical approach at the Hamiltonian, that fundamental processes are not included in the original von Neumann Equation.

To account for these neglected processes, we manually introduce the operator

$\hat{\rho}_s$ :

$$\partial_t \hat{\rho} = \frac{1}{i\hbar} [\hat{H}, \hat{\rho}] + \hat{\rho}_s. \quad (2.6)$$

We will attend to the explicit form of the additional operator later, after specifying the Hamiltonian.

Equation (2.6) is the Master Equation and describes the evolution of our system, e.g. nuclei interacting with radiation. Its main constituent is the Hamiltonian  $\hat{H}$ , which is presented in section 2.2.

The equations of motion following from Eq. (2.6) are also referred to as the Optical Bloch equations. They only describe a single particle interaction, i.e. they do not take the response of an expanded, many-particle solid-state sample into consideration. This will be done in section 2.5 by including the Maxwell-response of the medium and obtaining the MBE.

## 2.2 THE HAMILTONIAN

Let us now consider an incident energy field driving transitions in a quantum system with discrete energies, like in our investigated setup shown in figure 2 on page 9.

Due to the selection rules given in chapter 1, the radiation-nucleus interaction is limited to the four-level scheme shown in figure 3. In the Schrödinger picture, the system's total Hamiltonian can be written as

$$\hat{H} = \hat{H}_0 + \hat{H}_1, \quad (2.7)$$

with an unperturbed part  $\hat{H}_0$  and a perturbed one  $\hat{H}_1$ .

We assume the eigenvalues  $E_n$  of  $\hat{H}_0$  to be known and hence write it as

$$\hat{H}_0 = \sum_n E_n |\psi_n\rangle \langle \psi_n| = \sum_n \hbar\omega_n |n\rangle \langle n|, \quad (2.8)$$

with angular frequencies  $\omega_n$  and a simplified notation  $|\psi_n\rangle = |n\rangle$  of the n-th eigenstate.

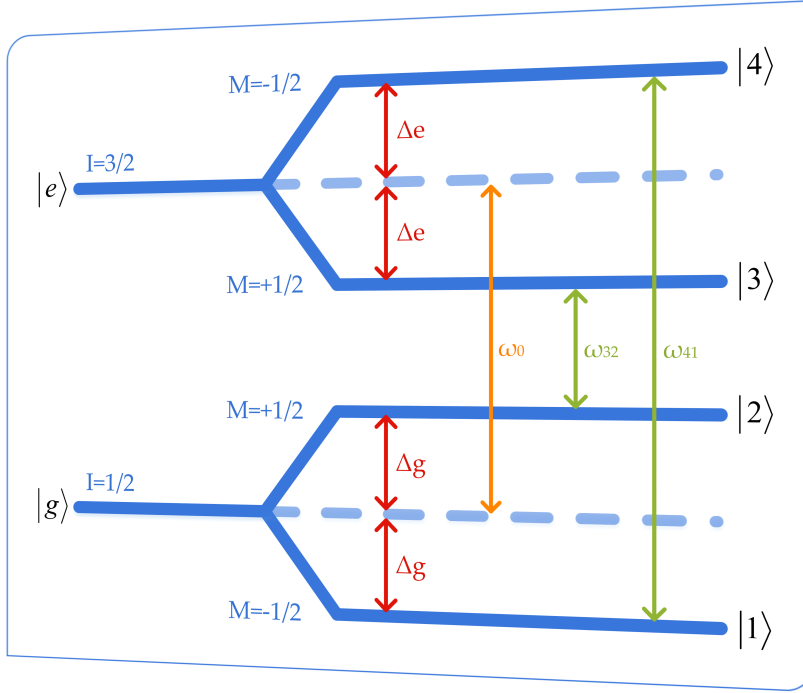


Figure 3: Schematic depiction of the four-level system in our ansatz. The ground  $|g\rangle$  and first excited state  $|e\rangle$  of  $^{57}\text{Fe}$  originally have six (degenerate) energy levels. The respective Zeeman splittings are denoted by  $\Delta g$  and  $\Delta e$ . Under the constraint of linearly polarized light in a certain B-field geometry, only the two  $\Delta M = 0$  transitions with  $M = \pm \frac{1}{2}$  are driven. The transition energy from the excited to the ground state is  $\omega_0 = 14.4$  keV.

The interaction part is given by the energy of the nuclear current  $\hat{\mathbf{j}}$  and charge  $\hat{\rho}_c$  in an external field, semi-classically described by a vector potential  $\mathbf{A}$  and a scalar potential  $\Phi$  [23]:

$$\hat{H}_1 = -\frac{1}{c}\hat{\mathbf{j}}(\mathbf{r}, t)\mathbf{A}(\mathbf{r}, t) + \hat{\rho}_c(\mathbf{r}, t)\Phi(\mathbf{r}, t). \quad (2.9)$$

To simplify this expression, we apply the Radiation Gauge for electro-magnetic fields (see Appendix A for the details). In this gauge, the scalar potential  $\Phi$  is zero, so that

$$\hat{H}_1 = -\frac{1}{c}\hat{\mathbf{j}}(\mathbf{r}, t)\mathbf{A}(\mathbf{r}, t). \quad (2.10)$$

## 2.3 OPTICAL BLOCH EQUATIONS

Let us now derive the optical Bloch equations, which arise from the Master Equation (2.6).

Our system's dynamics are therein determined by

$$i\hbar\partial_t\rho_{ij} - \rho_{ij}^s = \underbrace{\langle i | [\hat{H}, \hat{\rho}] | j \rangle}_{\textcircled{1}} + \underbrace{\langle i | [\hat{H}_1, \hat{\rho}] | j \rangle}_{\textcircled{2}}, \quad (2.11)$$

with  $\rho_{ij}^s$  denoting the  $ij$ -th matrix element of the spontaneous decay matrix.

The first right hand side term above equates to

$$\textcircled{1} \stackrel{(2.8)}{=} \sum_k \underbrace{\langle i | \hat{H}_0 | k \rangle}_{=\delta_{ik}\omega_i} \langle k | \hat{\rho} | j \rangle - \langle i | \hat{\rho} | k \rangle \underbrace{\langle k | \hat{H}_0 | j \rangle}_{=\delta_{kj}\omega_j} = \rho_{ij}(\omega_i - \omega_j). \quad (2.12)$$

For example from Fermi's Golden Rule we can see that the matrix element  $\langle i | \hat{H}_1 | j \rangle$  of the interaction Hamiltonian is proportional to the transition rate from state  $|j\rangle$  to  $|i\rangle$ .

Therefore we can conclude and define:

$$\langle i | \hat{H}_1 | j \rangle = \begin{cases} 0, & i \rightarrow j \text{ is a forbidden transition} \\ -\frac{\hbar}{2}\Omega_{ij}, & \text{otherwise (relabelling)}. \end{cases} \quad (2.13)$$

The fraction  $-\hbar/2$  was chosen to emphasize the matrix elements' connection to the Rabi frequency of a perturbed system.

In consequence, when considering the selection rule  $\Delta M = 0$  according to our setup that allows one transition  $t$  per state,  $|i\rangle \rightarrow |t(i)\rangle$ , and the system defined as in figure 3, the second term reads:

$$\textcircled{2} = -\frac{\hbar}{2}(\Omega_{it(i)}\rho_{t(i)j} - \rho_{it(j)}\Omega_{t(j)j}) \quad (2.14)$$

with the map

$$\frac{i}{t(i)} \begin{array}{c|c|c|c|c} |1\rangle & |2\rangle & |3\rangle & |4\rangle \\ \hline |4\rangle & |3\rangle & |2\rangle & |1\rangle \end{array}.$$

Seen that our final goal is to numerically solve the herefrom resulting equations, we conduct a phase transformation to get rid of fast oscillating terms that are contained within  $\Omega_{ij}$ :

$$\rho_{ij} \rightarrow \rho_{ij}e^{i\omega_L t} =: \rho'_{ij} \quad (2.15)$$

only for  $(ij) \in \{(31), (41), (32), (42)\} =: \text{Set}$ .

$\omega_L$  denotes the laser frequency.

This transformation is equivalent to making a change from the Schrödinger to an interaction picture frame [36].

If we define the unitary transform

$$U(t) := \begin{pmatrix} 1 & 0 & 0 & 0 \\ 0 & 1 & 0 & 0 \\ 0 & 0 & e^{-i\omega_L t} & 0 \\ 0 & 0 & 0 & e^{-i\omega_L t} \end{pmatrix}, \quad (2.16)$$

we may obtain a transform into a rotating frame just as defined in Eq. (2.15).

The density matrix then takes the form  $\hat{\rho}' = U^\dagger(t) \hat{\rho} U(t)$ , which equates to

$$\hat{\rho}' = \begin{pmatrix} \rho_{11} & \rho_{12} & e^{-i\omega_L t} \rho_{13} & e^{-i\omega_L t} \rho_{14} \\ \rho_{21} & \rho_{22} & e^{-i\omega_L t} \rho_{23} & e^{-i\omega_L t} \rho_{24} \\ e^{i\omega_L t} \rho_{31} & e^{i\omega_L t} \rho_{32} & \rho_{33} & \rho_{34} \\ e^{i\omega_L t} \rho_{41} & e^{i\omega_L t} \rho_{42} & \rho_{43} & \rho_{44} \end{pmatrix}. \quad (2.17)$$

Now, our ten equations read as follows:

I for  $(ij) \in \text{Set}$ :

$$\begin{aligned} i\hbar \partial_t \rho'_{ij} - \rho_{ij}^s = \\ \rho'_{ij}(\omega_i - \omega_j - \omega_L) - \frac{\hbar}{2} \left( e^{i\omega_L t} \Omega_{it(i)} \rho_{t(i)j} \right. \\ \left. - e^{i\omega_L t} \Omega_{t(j)j} \rho_{it(j)} \right), \end{aligned} \quad (2.18)$$

II for  $(ij) \notin \text{Set}$ :

$$\begin{aligned} i\hbar \partial_t \rho_{ij} - \rho_{ij}^s = \\ \rho_{ij}(\omega_i - \omega_j) - \frac{\hbar}{2} \left( e^{\text{sign}(t(i))\omega_L t} \Omega_{it(i)} \rho_{t(i)j} \right. \\ \left. - e^{\text{sign}(it(j))\omega_L t} \Omega_{t(j)j} \rho_{it(j)} \right), \end{aligned} \quad (2.19)$$

where

$$\text{sign}(t(i)j) := \begin{cases} +1, & \text{uneven} \\ -1, & \text{even permutation of } (ij) \in \text{Set}. \end{cases}$$

By studying the four-level system and the transition energies shown in figure 3, we can introduce the Zeeman splittings  $\Delta_e$ ,  $\Delta_g$  as well as the laser detuning  $\Delta := \omega_0 - \omega_L$  into our equation set. With  $\omega_i$  denoting the frequency corresponding to the energy level of state  $|i\rangle$ ,  $i \in \{1, 2, 3, 4\}$ , the explicit calculations are as follows:

- $\omega_2 - \omega_1 = 2\Delta g$ ,
- $\omega_3 - \omega_1 - \omega_L = \Delta g - \Delta e + \Delta$ ,
- $\omega_3 - \omega_2 - \omega_L = -(\Delta g + \Delta e) + \Delta$ ,
- $\omega_4 - \omega_1 - \omega_L = \Delta g + \Delta e + \Delta$ ,
- $\omega_4 - \omega_2 - \omega_L = \Delta e - \Delta g + \Delta$ ,
- $\omega_4 - \omega_3 = 2\Delta e$ .

With this setup we have arrived at the final Optical Bloch Equations. From this point, we will omit the prime in Eq. (2.18), so that  $\rho'_{ij} =: \rho_{ij}$ .

## 2.4 THE MATRIX ELEMENTS

So far in our equations above, we are looking at ten unknown  $\rho_{ij}$  matrix elements as well as  $\Omega_{ij} \propto \langle i | \hat{H}_1 | j \rangle$ .

To better describe the latter, but more importantly to obtain an expression for the scattered field amplitude of the incident radiation, we will exploit the radial symmetry of the nuclei to expand the interaction matrix elements into spherical waves.

This will provide us with a characterization of the incident photons by their multipolarity  $L$  and its projection  $M$  onto the quantization axis, in equivalence to their wave vector  $\mathbf{k}$  and polarization  $\sigma$  in a plane wave representation [27]. For this section, we mainly follow the arguments presented in Ref. [37] and

Ref. [38].

Initially, we expand the classical laser field in our perturbed Hamiltonian (section 2.2) in plane waves:

$$\mathbf{A} = \sum_{\mathbf{k}} \mathbf{A}_{\mathbf{k}} e^{i(\mathbf{k}\cdot\mathbf{r}-\omega_{\mathbf{k}}t)} + \text{c.c.}, \quad (2.20)$$

where we can drop the sum by restricting our scope to a single  $\mathbf{k}$  mode.

From the Maxwell Equations in Radiation Gauge ( $\Phi = 0$ ) we infer for the electric field  $\mathbf{E}$ :

$$\mathbf{E} = -\frac{1}{c} \partial_t \mathbf{A}. \quad (2.21)$$

Factorizing the fields into a slowly varying amplitude  $\mathbf{A}_{\mathbf{k}}(\mathbf{r}, t)$  and a rapidly oscillating part, we may arrive at

$$\begin{aligned} \mathbf{E}_{\mathbf{k}} e^{i(\mathbf{k}\cdot\mathbf{r}-\omega_{\mathbf{k}}t)} &= -\frac{1}{c} \left( -i\omega_{\mathbf{k}} \mathbf{A}_{\mathbf{k}} e^{i(\mathbf{k}\cdot\mathbf{r}-\omega_{\mathbf{k}}t)} + e^{i(\mathbf{k}\cdot\mathbf{r}-\omega_{\mathbf{k}}t)} (\partial_t \mathbf{A}_{\mathbf{k}}) \right) \\ &\approx \frac{i\omega_{\mathbf{k}}}{c} \mathbf{A}_{\mathbf{k}} e^{i(\mathbf{k}\cdot\mathbf{r}-\omega_{\mathbf{k}}t)} \end{aligned} \quad (2.22)$$

in the Rotating Wave Approximation [23].

Accordingly, by writing the polarization vector  $\mathbf{e}_{\mathbf{k}\sigma}^*$  explicitly, we have

$$\mathbf{A}(\mathbf{r}, t) = \mathbf{A}_{\mathbf{k}}(\mathbf{r}, t) e^{i(\mathbf{k}\cdot\mathbf{r}-\omega_{\mathbf{k}}t)} + \text{c.c.} \approx \frac{-ic}{\omega_{\mathbf{k}}} E_{\mathbf{k}}(\mathbf{r}, t) \mathbf{e}_{\mathbf{k}\sigma}^* e^{i(\mathbf{k}\cdot\mathbf{r}-\omega_{\mathbf{k}}t)} + \text{c.c.} \quad (2.23)$$

From this we find for the matrix elements

$$\begin{aligned} \langle f | \hat{H}_1 | i \rangle &= -\frac{1}{c} \langle f | \hat{\mathbf{j}} \cdot \mathbf{A} | i \rangle \\ &\approx \frac{i}{\omega_{\mathbf{k}}} \int_V \mathbf{j}(\mathbf{r}, t) \cdot E_{\mathbf{k}}(\mathbf{r}, t) \mathbf{e}_{\mathbf{k}\sigma}^* e^{i(\mathbf{k}\cdot\mathbf{r}-\omega_{\mathbf{k}}t)} d^3\mathbf{r} + \text{c.c.} \\ &\stackrel{*}{\approx} \frac{i}{\omega_{\mathbf{k}}} e^{-i\omega_{\mathbf{k}}t} E_{\mathbf{k}} \int_V \mathbf{j}(\mathbf{r}, t) \mathbf{e}_{\mathbf{k}\sigma}^* e^{i\mathbf{k}\cdot\mathbf{r}} d^3\mathbf{r} + \text{c.c.} \end{aligned} \quad (2.24)$$

where in (\*) we have used that  $E_{\mathbf{k}}$  is a slowly varying envelope and hence sufficiently constant over the vicinity of the integral.

Let us now proceed to expressing the integrand of Eq. (2.24) by the means of spherical waves.

Following the formalism described in Refs. [37], [38] and [39], we can for-

ulate the interaction matrix elements employing electric  $\mathcal{E}$  and magnetic  $\mathcal{M}$  multipole fields:

$$\mathbf{j}(\mathbf{r}, t) \mathbf{e}_{\mathbf{k}\sigma}^* e^{i\mathbf{k}\cdot\mathbf{r}} = \sum_{L,M} \sqrt{2\pi(2L+1)} (-i)^L \mathcal{D}_{M,-\sigma}^L(\mathbf{k}) (i\sigma \mathbf{A}_{LM}^{\mathcal{E}}(\mathbf{r}) + \mathbf{A}_{LM}^{\mathcal{M}}(\mathbf{r})), \quad (2.25)$$

with the Wigner rotation matrix  $\mathcal{D}_{M,-\sigma}^L(\mathbf{k})$  [31] turning the quantization axis ( $\hat{y}$ ) into the direction of  $\mathbf{k}$ .

Considering only the case of incident photons already parallel to the quantization axis, no rotation is needed, so that  $\mathcal{D}_{M,-\sigma}^L(\mathbf{k}) = \delta_{M,-\sigma}$  now reduces to selecting the desired polarization, for which we can execute the sum over  $M$ .

The multipole fields  $\mathbf{A}_{LM}^{\mathcal{E}/\mathcal{M}}(\mathbf{r})$  are given by

$$\begin{aligned} \mathbf{A}_{LM}^{\mathcal{E}}(\mathbf{r}) &= \sqrt{\frac{L+1}{2L+1}} j_{L-1}(kr) \mathbf{Y}_{LL-1}^M(\theta, \phi) - \sqrt{\frac{L}{2L+1}} j_{L+1}(kr) \mathbf{Y}_{LL+1}^M(\theta, \phi) \\ &= -\frac{i}{k} \nabla \times (j_L(kr) \mathbf{Y}_{LL}^M(\theta, \phi)) \\ &\text{and} \\ \mathbf{A}_{LM}^{\mathcal{M}}(\mathbf{r}) &= j_L(kr) \mathbf{Y}_{LL}^M(\theta, \phi). \end{aligned} \quad (2.26)$$

$\mathbf{Y}_{LL}^M(\theta, \phi)$  are the vector spherical harmonics and  $j_L(kr)$  the  $L$ -th spherical Bessel function.

Eq. (2.24) now reads

$$\begin{aligned} \langle f | \hat{H}_1 | i \rangle &\approx \frac{i\mathbf{E}_k}{\omega_k} e^{-i\omega_k t} \sum_L \sqrt{2\pi(2L+1)} (-i)^L \\ &\times \int_V \mathbf{j}(\mathbf{r}) \left( \frac{-i\sigma}{k} \nabla \times (j_L(kr) \mathbf{Y}_{LL}^{-\sigma}(\theta, \phi)) + j_L(kr) \mathbf{Y}_{LL}^{-\sigma}(\theta, \phi) \right) \end{aligned} \quad (2.27)$$

Since the radiation wave length  $\lambda$  is much larger than the nuclear radius  $R_n$  the product  $\frac{2\pi}{\lambda} R_n = kR_n \ll 1$  becomes sufficiently small to justify an expansion of  $j_L(kr)$  in  $kr$  up to the first order. This is known as the long-wavelength approximation [38].

Involving the definitions of the electric  $\mathbf{Q}_{LM}$  and the magnetic  $\mathbf{M}_{LM}$  multipole



moment operators as [38]

$$\begin{aligned} Q_{LM} &= \int r^L Y_{LM}^*(\theta, \phi) \rho(\mathbf{r}) d^3r, \\ \mathbb{M}_{LM} &= \frac{1}{c(L+1)} \int [\mathbf{r} \times \mathbf{j}(\mathbf{r})] \nabla (r^L Y_{LM}^*(\theta, \phi)) d^3r, \end{aligned} \quad (2.28)$$

our matrix elements take the form [27]

$$\begin{aligned} \langle f | \hat{H}_1 | i \rangle &= -E_k e^{-i\omega_k t} \sqrt{2\pi} \sum_L (-i)^{L+1} \sqrt{\frac{(2L+1)(L+1)}{L}} \\ &\quad \times \frac{\sigma k^{L-1}}{(2L+1)!!} \langle f | Q_{L-\sigma} | i \rangle \end{aligned} \quad (2.29)$$

in the case of electric transitions and

$$\begin{aligned} \langle f | \hat{H}_1 | i \rangle &= -E_k e^{-i\omega_k t} \sqrt{2\pi} \sum_L (-i)^L \sqrt{\frac{(2L+1)(L+1)}{L}} \\ &\quad \times \frac{k^{L-1}}{(2L+1)!!} \langle f | \mathbb{M}_{L-\sigma} | i \rangle \end{aligned} \quad (2.30)$$

in the case of magnetic transitions.

Thereby,  $n!!$  marks the double factorial, i.e.  $n!! = n \cdot (n-2) \cdot (n-4) \cdot \dots$

So far, we reduced our interaction Hamiltonian to the calculation of the respective matrix elements of the electric and magnetic multipole moment operators. Exploiting that these operators are spherical tensors, we can apply the Wigner-Eckart theorem [31] to split off the dependency on the magnetic quantum number  $M$ ,  $-\sigma$ :

$$\langle f | \mathbb{T}_{LM} | i \rangle = \frac{(-1)^{I_i - M_i}}{\sqrt{2L+1}} C(I_f I_i L; M_f - M_i M) \langle f || \mathbb{T}_L || i \rangle \quad (2.31)$$

for the  $M$ -th component of a spherical tensor  $\mathbb{T}_{LM} = \mathbb{E}_{LM}/\mathbb{M}_{LM}$  of rank  $L$ . The constants  $C(j_1 j_2 J; M_1 M_2 M)$  denote the Clebsch-Gordan coefficients and  $I_i$ ,  $M_i$  the spin of state  $|i\rangle$  and its projection.

$\langle f || \cdot || i \rangle$  is commonly referred to as the reduced matrix element, despite not being an actual scalar product from the projection onto  $\langle f |$  and  $|i\rangle$  in the strict mathematical sense.

Now that our multipole operator matrix elements are independent of the angular momentum substructure, we can relate them to the principal transition

probabilities

$$\mathcal{B}(\mathcal{E}/\mathcal{M}L, I_i \rightarrow I_f) = \frac{1}{2I_i + 1} |\langle f | \hat{Q}_L / \mathbb{M}_L | i \rangle|^2 \quad (2.32)$$

and finally arrive at

$$\begin{aligned} \langle f | \hat{H}_1 | i \rangle &= E_k e^{-i\omega_k t} (-1)^{I_i - M_i} (-i)^{L+1} \sigma \sqrt{(2I_i + 1)} C(I_f I_i L; M_f - M_i - \sigma) \\ &\quad \times \underbrace{\sqrt{\frac{2\pi(L+1)}{L}} \frac{k^{L-1}}{(2L+1)!!} \sqrt{\mathcal{B}(\mathcal{E}L, I_i \rightarrow I_f)}}_{=:\alpha(\mathcal{E}L, I_i \rightarrow I_f)} \end{aligned} \quad (2.33)$$

in the case of electric transitions and constraining our system to only one multipolarity  $L$ .

We have chosen the definition of the multipole moment  $\alpha(\mathcal{E}L, I_i \rightarrow I_f)$  as in Ref. [40].

With the magnetic transitions elements differing just by scaling or phase factors from the electric, we can summarize:

$$\langle f | \hat{H}_1 | i \rangle \sim e^{-i\omega_k t} E_k(z, t) (-1)^{I_i - M_i} C(I_f I_i L; M_f - M_i - \sigma) \alpha(\mathcal{E}/\mathcal{M}L, I_i \rightarrow I_f), \quad (2.34)$$

where we amended  $E_k(\mathbf{r}, t) = E_k(z, t)$  according to a unidirectional propagation along the  $z$ -axis.

## 2.5 THE WAVE EQUATION

As of now, we have neglected in our considerations the response the incident radiation generates in the expanded solid-state sample.

To include this in our model, we turn to the Maxwell equations in matter to find a wave equation for our radiation. As this equation imposes another condition for the sought solution, we aim to couple it to the other conditions (2.18) and (2.19). Doing so can be achieved by linking the wave equations source term to the density matrix and Rabi frequencies.

The (macroscopic) Maxwell equations read

$$\begin{aligned} \text{i) } \operatorname{div} \mathbf{D} &= 4\pi\rho \stackrel{\rho=0}{=} 0 & \text{ii) } \operatorname{div} \mathbf{B} &= 0 \\ \text{iii) } \operatorname{rot} \mathbf{E} &= -\frac{1}{c} \partial_t \mathbf{B} & \text{iv) } \operatorname{rot} \mathbf{H} &= \frac{1}{c} (4\pi \mathbf{J} + \partial_t \mathbf{D}), \end{aligned} \quad (2.35)$$

with the displacement and magnetizing fields  $\mathbf{D} = \mathbf{E} + 4\pi\mathbf{P}$ ,  $\mathbf{H} = \mathbf{B} - 4\pi\mathbf{M}$  and polarization  $\mathbf{P}$  as well as magnetization  $\mathbf{M}$  of the medium.

The vector  $\mathbf{J}$  corresponds to the free macroscopic current density, i.e. the current induced by the light in the sample.

With  $\mathbf{P}$ ,  $\mathbf{M}$  set to zero, we obtain for the electric field [41]:

$$\begin{aligned} \text{iii) } \implies \operatorname{rot} \operatorname{rot} \mathbf{E} &= -\frac{1}{c} \partial_t \operatorname{rot} \mathbf{B} \\ \implies (-c^2 \Delta + \partial_t^2) \mathbf{E} + 4\pi \mathbf{J} &= 0, \end{aligned} \quad (2.36)$$

or in one dimension

$$\left( \partial_z^2 - \frac{1}{c^2} \partial_t^2 \right) \mathbf{E} = \frac{4\pi}{c^2} \mathbf{J}, \quad (2.37)$$

from which we can see, that the wave equation has  $\mathbf{J}$  as source term.

Like above, we are assuming an electro-magnetic wave unidirectionally propagating in forward  $z$ -direction, which is now assumed to be linearly polarized along the  $x$ -axis:

$$\mathbf{E}(z, t) = E(z, t) e^{i(k \cdot z - \omega_k t)} \mathbf{e}_x, \quad (2.38)$$

with slowly varying envelope (SVE)  $E(z, t)$  and optical dispersion relation  $k = \frac{\omega_k}{c}$ .

Writing the current as  $\mathbf{J}(z, t) = J(z, t) e^{i(k \cdot z - \omega_k t)} \mathbf{e}_x$ , like proposed in Ref. [40], we can find for Eq. (2.37):

$$\begin{aligned} \left( \partial_z^2 + 2ik\partial_z - \frac{1}{c^2} \partial_t^2 + 2\frac{i\omega_k}{c^2} \partial_t \right) E(z, t) &= \frac{4\pi}{c^2} (-i\omega_k + \partial_t) J(z, t) \\ \implies \left( \partial_z + \frac{1}{c} \partial_t \right) E(z, t) &= -\frac{2\pi}{c} J(z, t). \end{aligned} \quad (2.39)$$

Considering the slow propagation of the envelopes in time as well as in space, we note that for the respective highest order derivatives it is assumed that  $|\partial_z^2 E| \ll |k\partial_z E|$ ,  $|\partial_t^2 E| \ll |\omega_k \partial_t E|$  and  $|\partial_t J| \ll |\omega_k J|$ , which is why we applied the SVE approximation to retrieve Eq. (2.39).

According to Ref. [40], the current density for a single nuclear resonance may be obtained by summing over all nuclei involved in the coherent scattering and tracing over  $\hat{\mathbf{j}}(\mathbf{k})e^{-ikz}\hat{\rho}$ .

We exploit that, here,  $\hat{\mathbf{j}}(\mathbf{k})$  is the nuclear deexcitation current operator in momentum space, meaning that the terms of  $\langle j | \hat{\mathbf{j}} | i \rangle$  vanish or can be neglected except if  $|i\rangle \rightarrow |j\rangle$  is a deexciting transition participating in the coherent scattering in the observed system [42].

Rewriting the source term accordingly yields:

$$\begin{aligned} J(z, t)\mathbf{e}_x &= N \operatorname{tr}(\hat{\mathbf{j}}e^{-ikz}\hat{\rho}) = N \sum_{i=1}^4 \langle i | \hat{\mathbf{j}}e^{-ikz}\hat{\rho} | i \rangle \\ &\stackrel{(*)}{=} N \sum_{i, h} \underbrace{\langle i | \hat{\mathbf{j}} | h \rangle}_{\text{selection rules}} \langle h | e^{-ikz}\hat{\rho} | i \rangle \\ &= N(\langle 1 | \hat{\mathbf{j}}e^{-ikz} | 4 \rangle \rho_{41} + \langle 2 | \hat{\mathbf{j}}e^{-ikz} | 3 \rangle \rho_{32}), \end{aligned} \quad (2.40)$$

where in (\*) we have inserted the identity  $\mathbb{1} = \sum_h |h\rangle \langle h|$  and  $N$  denotes the particle number density.

When taking into account the form of  $\hat{H}_1$  from Eq. (2.24), but also in momentum space,  $\hat{H}_1 = \frac{i}{\omega_k} \hat{\mathbf{j}}^*(\mathbf{k})E_k(z, t)\mathbf{e}_x e^{i(kz - \omega_k t)}$  [28], the wave equation fully connects to the optical Bloch equations by:

$$\begin{aligned} \left( \partial_z + \frac{1}{c} \partial_t \right) E_k(z, t) &= -\frac{2\pi}{c} J(z, t) \\ &= -\frac{2\pi}{c} N (\langle 1 | \hat{\mathbf{j}}e^{-ikz} | 4 \rangle \rho_{41} + \langle 2 | \hat{\mathbf{j}}e^{-ikz} | 3 \rangle \rho_{32}) \mathbf{e}_x \\ &= -\frac{2\pi\omega_k}{ic} \frac{N}{E_k(z, t)} \left( e^{i\Delta t} \langle 4 | \hat{H}_1 | 1 \rangle \rho_{41} \right. \\ &\quad \left. + e^{i\Delta t} \langle 3 | \hat{H}_1 | 2 \rangle \rho_{32} \right), \end{aligned} \quad (2.41)$$

where in the last step, we phase-transformed  $\hat{\rho}_{ij}$  as in Eq. (2.15) in section 2.3 and introduced the transition-laser detuning  $\Delta := \omega_k - \omega_L$ .

In consideration of Eq. (2.34), we adjust our definition of the Rabi frequency to absorb the phase factor  $e^{i\Delta t} \Omega_{ij} =: \tilde{\Omega}_{ij}$ . We find this phase factor in our equations listed right here, but also in the OBE.

The wave equation now reads:

$$\left(\partial_z + \frac{1}{c}\partial_t\right)\Omega(z, t) = \frac{i2\pi\omega_k}{\hbar c}N \times \alpha^2(\mathcal{E}/\mathcal{ML}, I_g \rightarrow I_e)((-1)^{I_g - M_1}C_{41} \cdot \rho_{41} + (-1)^{I_g - M_2}C_{32} \cdot \rho_{32}) \quad (2.42)$$

while employing the Clebsch-Gordan coefficients  $C_{fi} := C(I_f I_i L, M_f - M_i M)$  as before and merging all matrix elements by defining  $E_k(z, t)\alpha(\mathcal{E}/\mathcal{ML}, I_i \rightarrow I_f) = \frac{\Omega_{fi}}{\pm C_{fi}} =: \Omega(z, t)$ .

Consider that  $\alpha$  is independent of the magnetic degeneration,  $\alpha(I_1 \rightarrow I_4) = \alpha(I_2 \rightarrow I_3) = \alpha(I_g \rightarrow I_e)$  with  $g, e$  denoting the ground and excited state in our setup (fig. 3).

Together with the OBE, we now accomplished the derivation of the MBE.

The values of the reduced transition probabilities  $\mathcal{B}(\mathcal{E}/\mathcal{ML}, I_g \rightarrow I_e)$  are available from experimental determination.

For the purpose of convenience we now rewrite Eq. (2.42) following Ref. [40] so that we can replace  $\mathcal{B}/\alpha$  by parameters we would like to manipulate in our setup.

$$\alpha^2(\mathcal{E}/\mathcal{ML}, I_g \rightarrow I_e) = \frac{\hbar\Gamma\sigma_r}{8\pi k}, \quad (2.43)$$

with the resonant cross section  $\sigma_r$ .

Exploiting the dispersion relation  $\omega_k/k = c$ , introducing the sample's optical thickness  $\xi := N\sigma L/4$  and defining  $\eta := \xi\Gamma/L$ , we obtain the final wave equation in the simplified form

$$\left(\partial_z + \frac{1}{c}\partial_t\right)\Omega(z, t) = i\eta(C_{32} \cdot \rho_{32}(z, t) - C_{41} \cdot \rho_{41}(z, t)). \quad (2.44)$$

We also implemented  $|I_g M_1\rangle = |1/2 - 1/2\rangle$ ,  $|I_g M_2\rangle = |1/2 1/2\rangle$  specific to our  $^{57}\text{Fe}$  system to evaluate  $(-1)^{I_g - M_g}$ .

## 2.6 DECOHERENCE MATRIX

As mentioned in sec. 2.1, in the general case, the occurring decoherence processes that are not included in the Hamiltonian, may be accounted for by the

introduction of a decoherence matrix  $\hat{\rho}_s$ . Let us now see, what this means for our specific system.

Phenomenologically, one can observe a spontaneous decay of the populations of the excited states and coherences [41]. Spontaneous emission depends upon quantum mechanical vacuum fluctuations and cannot be explained by classical physics.

Since we chose a classical description of the incident radiation, these processes are neglected by our Hamiltonian. We therefore set  $\hat{\rho}_s$  to account for the spontaneous decay in our system.

As illustrated in figure 4, the populations of the excited states  $\rho_{44}$ ,  $\rho_{33}$  decay with corresponding rates  $\gamma_{ij}$  ( $i = 3,4$  and  $j = 1,2$ ) into the ground state populations  $\rho_{22}$ ,  $\rho_{11}$ .

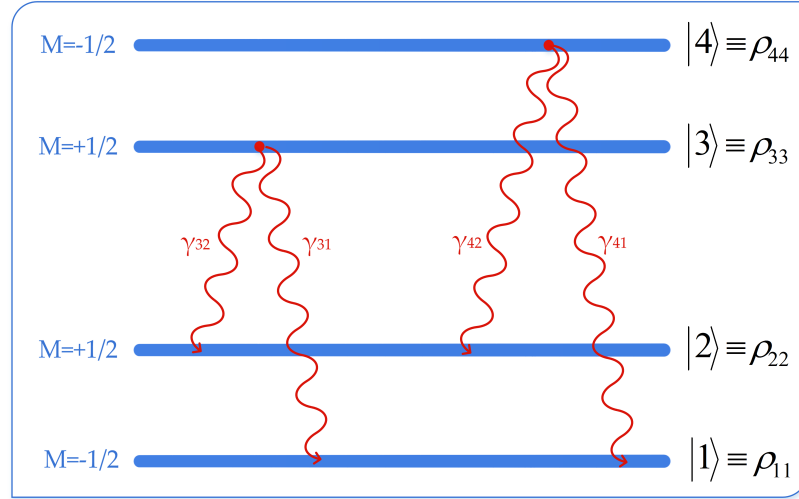


Figure 4: Schematic depiction of the decay processes in the four-level system of our ansatz. The excited state populations  $\rho_{44}$ ,  $\rho_{33}$  decay into the ground states.

The coherences  $\rho_{ij}, i \neq j$ , represent the magnitude of well-defined, constant phase relation, i.e. coherence, caused by the external energy field (the laser) between state  $|i\rangle$  and all states it has coherence with. They decay with rates  $\sum_j \gamma_{ij}/2$  [41].

Following these arguments leads to a  $\hat{\rho}_s$  in matrix form of [23]:

$$\begin{pmatrix} \gamma_{31}\rho_{33} + \gamma_{41}\rho_{44} & 0 & -1/2(\gamma_{31} + \gamma_{32})\rho_{13} & -1/2(\gamma_{41} + \gamma_{42})\rho_{14} \\ 0 & \gamma_{32}\rho_{33} + \gamma_{42}\rho_{44} & -1/2(\gamma_{31} + \gamma_{32})\rho_{23} & -1/2(\gamma_{41} + \gamma_{42})\rho_{24} \\ -1/2(\gamma_{31} + \gamma_{32})\rho_{31} & -1/2(\gamma_{31} + \gamma_{32})\rho_{32} & (\gamma_{32} + \gamma_{31})\rho_{33} & -1/2(\gamma_{31} + \gamma_{32})\rho_{34} \\ -1/2(\gamma_{41} + \gamma_{42})\rho_{41} & -1/2(\gamma_{41} + \gamma_{42})\rho_{42} & -1/2(\gamma_{41} + \gamma_{42})\rho_{43} & (\gamma_{42} + \gamma_{41})\rho_{44} \end{pmatrix}.$$

Using the Clebsch-Gordan coefficients  $C(j_1 j_2 J, M_1 M_2 M)$  and the spin  $(I_g, I_e)$  as well as magnetic quantum numbers  $(M_g, M_e)$ , we can relate the partial decay rates to the total decay rate  $\Gamma$  of the system [27]:

$$\gamma_{ji} = \frac{2I_e + 1}{2L + 1} C^2(I_g I_e L, M_g - M_e M) \Gamma =: \frac{2I_e + 1}{2L + 1} C_{ij}^2 \Gamma, \quad (2.45)$$

where we let  $i$  set the quantum numbers of the ground state  $g$ , and  $j$  the ones of the excited state  $e$ . Thereby,  $C_{ij}$  equals  $C(I_i I_j L, M_i - M_j M)$  with the state  $|j\rangle$  defined as  $|I_e M_e\rangle$  and  $|i\rangle$  as  $|I_g M_g\rangle$ .  $L$  depicts the multipolarity of the decay photon.

We will denote  $\frac{2I_e + 1}{2L + 1} =: \beta$  in the subsequent MBE (Eq. (2.46)).

## 2.7 MAXWELL-BLOCH EQUATIONS

As we have done all the preparations in the section before, we are just left with combining our previous findings.

In summary: the MBE consider not only the system dynamics arising directly from QM via Eq. (2.6), but also include the spontaneous decay (section 2.6) as well as the response the incident radiation generates in the sample.

To obtain the form below, we exploit that  $C(I_e I_g 1; M_e - M_g M) = C(I_g I_e 1; M_g - M_e M)$  with the respective ground ( $g$ ) and excited ( $e$ ) state level angular momenta of our system, and honoured the scaling factor  $(-1)^{I_g - M_g}$  from equation (2.34).

$$\begin{aligned}
\partial_t \rho_{11} &= \beta\Gamma(C_{31}^2 \rho_{33} + C_{41}^2 \rho_{44}) - i/2 C_{41}(\Omega^* \rho_{41} - \Omega \rho_{14}), \\
\partial_t \rho_{21} &= -2i\Delta_g \rho_{21} + i/2(C_{32}\Omega^* \rho_{31} + C_{41}\Omega \rho_{24}), \\
\partial_t \rho_{31} &= -\beta\Gamma/2(C_{31}^2 \rho_{31} + C_{31}^2 \rho_{31}) - i(\Delta_g - \Delta_e + \Delta)\rho_{31} \\
&\quad + i/2\Omega(C_{32}\rho_{21} + C_{41}\rho_{34}), \\
\partial_t \rho_{41} &= -\beta\Gamma/2(C_{41}^2 + C_{42}^2)\rho_{41} - i(\Delta_e + \Delta_g + \Delta)\rho_{41} - i/2 C_{41}\Omega(\rho_{11} - \rho_{44}), \\
\partial_t \rho_{22} &= \beta\Gamma(C_{32}^2 \rho_{33} + C_{42}^2 \rho_{44}) + i/2 C_{32}(\Omega^* \rho_{32} - \Omega \rho_{23}), \\
\partial_t \rho_{32} &= -\beta\Gamma/2(C_{31}^2 + C_{42}^2)\rho_{32} - i(\Delta - (\Delta_g + \Delta_e))\rho_{32} + i/2 C_{32}\Omega(\rho_{22} - \rho_{33}), \\
\partial_t \rho_{42} &= -\beta\Gamma/2(C_{41}^2 + C_{42}^2)\rho_{42} - i(\Delta_e - \Delta_g + \Delta)\rho_{42} - i/2\Omega(C_{41}\rho_{12} + C_{32}\rho_{43}), \\
\partial_t \rho_{33} &= -\beta\Gamma(C_{32}^2 + C_{31}^2)\rho_{33} + i/2 C_{32}(\Omega \rho_{23} - \Omega^* \rho_{32}), \\
\partial_t \rho_{43} &= -\beta\Gamma/2(C_{41}^2 + C_{42}^2)\rho_{43} - i2\Delta_e \rho_{43} - i/2(C_{41}\Omega \rho_{13} + C_{32}\Omega^* \rho_{42}), \\
\partial_t \rho_{44} &= -\beta\Gamma(C_{41}^2 + C_{42}^2)\rho_{44} - i/2 C_{41}(\Omega \rho_{14} - \Omega^* \rho_{41}), \\
\left(\partial_z + \frac{1}{c}\partial_t\right)\Omega(z, t) &= i\eta(C_{32} \cdot \rho_{32}(z, t) - C_{41} \cdot \rho_{41}(z, t)).
\end{aligned} \tag{2.46}$$

By solving the above equations for the matrix element  $\Omega(z, t) \sim E_k(z, t)$  we expect to find the amplitude of our radiation as and after it passes through the grid of nuclei.

As initial conditions we choose:

- The initial populations are 50% in each of the two ground states  $\rho_{11}$ ,  $\rho_{22}$  while all other  $\rho_{ij}$  are set to zero.
- The incident radiation is given by an ultrashort pulse, which we smooth, for computational purposes, to a Gaussian of width  $\tau = 1\text{ns}$  (in intensity) that is reaching the sample at  $10\tau$ :  $\Omega(0, t) = \exp\left(-\frac{(t-10\tau)^2}{\tau}\right)$ .



## Part II

### NUMERICAL RESULTS

This part presents the numerical results of this thesis. It begins with the reproduction of two fundamental effects utilized and then shows the new findings. It concludes with a summary and outlook.



## COHERENT PHOTON STORAGE AND PHASE MODULATION

---

In figure 2 on page 9, we have specified a setup, in which an x-ray pulse impinges on a probe of  $^{57}\text{Fe}$  Mößbauer nuclei. The pulse is tuned to the 14.4 keV M1 transition and due to its sufficient width, it addresses all six transitions between the six magnetic sublevels. However, only the two  $\Delta M = 0$  transitions are driven as a consequence of the combination of the linear pulse polarization and the choice of the quantization axis (cf. sec. 1.2 on page 8). The external magnetic field determining that axis permeates the sample and can be switched on and off as well as inverted.

This chapter is dedicated to explaining the fundamental behaviour of the forward scattered electric field in the time spectrum. Furthermore, we reproduce the results of Ref. [1], which presented the coherent photon storage and phase modulation via magnetic switching.

### 3.1 RESONANTLY SCATTERED FIELD AMPLITUDE

The dynamics of our incident electric field, as it passes through the sample, are given by  $\Omega(z, t)$  from sec. 2.7. Being interested in the forward scattered intensity detectable behind the sample, we view  $\Omega$ 's time evolution at the end  $z = L$  of the medium.

Figure 5.i) illustrates the unperturbed time spectrum dynamics with and without Zeeman splitting, as they are explained in the following. The plot shows our results from numerically solving the MBE derived in chapter 2 for optical thicknesses  $\xi = 60$ ,  $\xi/2 = 30$ , magnetic fields  $B = 34.4$  T,  $B = 0$  T and a time range of 600 ns.

*Dynamics without Zeeman Splitting*

In the absence of any external magnetic field, only the two degenerate energy levels of each the ground and first excited state of our specified nucleus system  $^{57}\text{Fe}$  are within relevant scope of the laser. The laser can therefore drive only this one transition between the two levels.

Reflecting the driving of a single transition, one could expect to see only a natural, spontaneous decay  $\Omega \sim e^{-\Gamma t}$  of the unstable excited state.

However: our equations contain the optical thickness  $\xi$ , defined in sec. 2.5 on page 27, which is proportional to the number of nuclei in the sample. As we choose a sufficiently large thickness, the resonant photon gets reabsorbed and emitted by several nuclei before leaving the medium. This is referred to as the "Multiple Scattering Effect".

The recoilless absorption of the photon leads to a re-emission within the line width of the just driven transition (see sec. 1.2). Thereby, its remaining energy is sufficient to again drive this same transition. As this effect may sequentially happen with multiple nuclei before the beam leaves the sample, the scattered radiation arises from a superposition of multiple scattering processes. The interference of this superposition constructs a pattern called Dynamical Beat, which is shown in figure 5.

An analytic solution of this Dynamical Beat via the first Bessel function  $J_1$  is provided as [23]

$$|\Omega_0(L, t)|^2 \sim \left( \frac{\xi}{\sqrt{\xi\Gamma t}} J_1(2\sqrt{\xi\Gamma t}) \right)^2 e^{-\Gamma t},$$

which is proportional to  $\frac{1}{\xi\Gamma}$  at short times. We obtain the same dynamics by numerically solving our system of PDE (2.46) for  $B = 0$ .

As  $\xi$  grows, so does the frequency of oscillations in  $\Omega_0$ . Nonetheless, the overall lifetime of these dynamics is naturally limited by the spontaneous decay  $e^{-\Gamma t}$ .

*Dynamics with Zeeman Splitting*

Immersing the nuclei in a non-vanishing magnetic field removes the degeneracy from the energy levels, so that the ground state splits into two and the

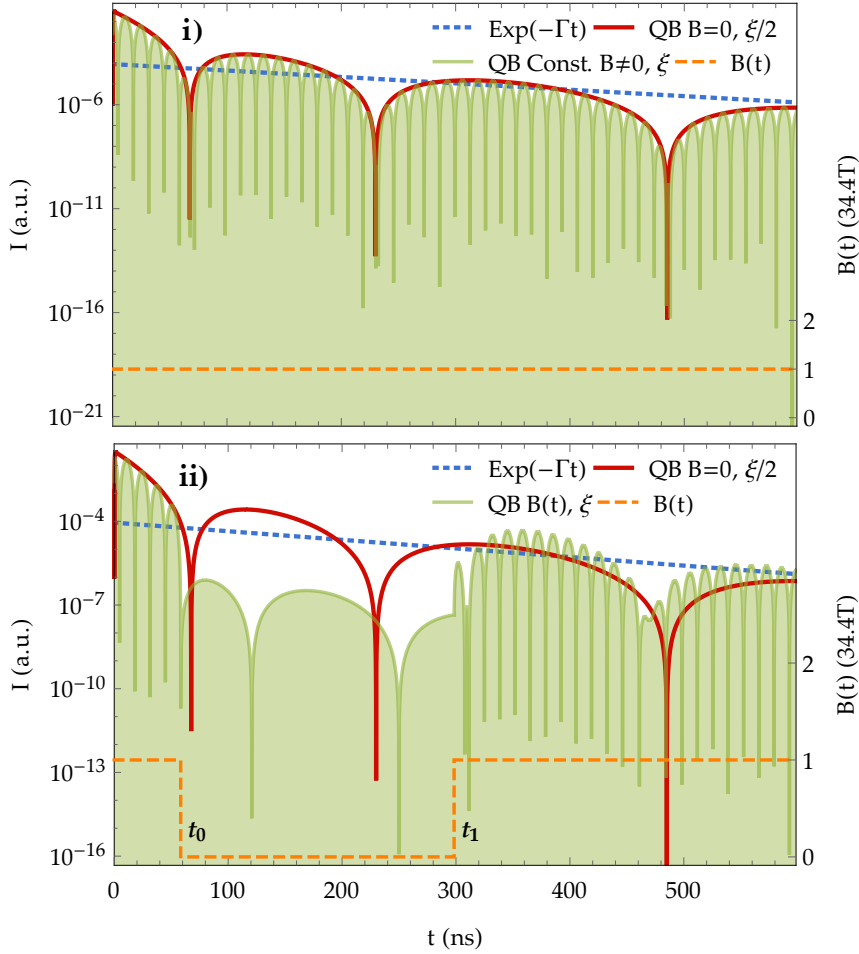


Figure 5: **i)** Quantum beat of the  $\Delta M = 0$  transitions (green line) for a constant magnetic field  $B = 34.4$  T and optical thickness  $\xi = 60$ . The corresponding envelope (red line) is given by the Dynamical Beat calculated for  $B = 0$  and  $\xi = 30$ . See text for further explanations. **ii)** Coherent storage effect between  $t_0$  and  $t_1$ , the storage time can be arbitrarily chosen and was set to  $\tau_{\text{off}} = 240$  ns. In both plots we used an optical thickness of  $\xi = 60$  and  $\xi/2 = 30$  respectively.

excited into four distinctive sublevels. We end up in our known four-level scheme (figure 3 on page 17) by choosing a geometry in which the selection rule  $\Delta M = 0$  forbids all but two transitions. Now, both of these transitions are driven by the laser.

Again, rooted in the delocalized nature of the Nuclear Exciton, we observe an interference. Though, this time, not only of multiple scatterings, but additionally of the two transitions  $\hbar\omega_{32}$  and  $\hbar\omega_{41}$  via which the x-ray photon scatters. This holds as long as we only detect the total photon count behind the sample and do not resolve the detected radiation in the energy spectrum. The carrier oscillations are governed by the beat of  $\omega_{32}$  and  $\omega_{41}$ , called Quantum Beat

(QB).

The envelope dynamics is still given by the multiple scatterings and therefore the Bessel-function. We note here that for the same optical thickness  $\xi$ , the Dynamical Beat (for the case of  $B = 0$ ) does not represent the QB envelope. We can see in figure 5 that the optical thickness is  $\xi$  for the QB and only  $\xi/2$  for the Dynamical Beat that illustrates its envelope. The pace of the Dynamical Beat (for  $B = 0$ ) is connected to the number of nuclei in the same ground state via the multiple scattering. In case of  $B = 0$ , the number of resonant nuclei is assumed to be  $N$ . Since the ground state splits into two Zeeman levels for  $B \neq 0$  and the populations distribute equally at room temperature, only  $N/2$  nuclei contribute to the resonant scattering for each of the two  $\Delta M = 0$  transitions. As a result, at the same  $\xi$ , the QB envelope oscillates slower than the Dynamical Beat corresponding to the pure two-level system in the absence of any magnetic field.

Since  $\xi$  is proportional to the number of nuclei (see the definition on page 27), we compensate for this effect by halving  $\xi$  for the envelope plot.

The angular beat frequency  $\omega_{QB}$  is

$$\frac{\omega_{41} - \omega_{32}}{2} = \frac{(\omega_4 - \omega_1) - (\omega_3 - \omega_2)}{2} \quad (3.1)$$

$$\stackrel{\text{fig. 3}}{=} \Delta_e + \Delta_g = \Delta_{B_0} = \omega_{QB}.$$

We may infer from the amplitude dynamics that two beats make up one period  $T_{QB}$ . Hence, we witness one lobe every  $T_{QB}/2 = \pi/\Delta_{B_0}$  time steps. In case the envelope (Dynamical Beat for half  $\xi$ ) and beat minima would not coincide, the QB regularity is broken so that the lobes can be squeezed into the envelope and the minima do coincide. This squeezing effect is visible in figure 5.i) around the dynamical beat minima.

With the Zeeman splittings being proportional to the magnetic field strength, we can narrow the QB pattern by increasing  $B$ . Throughout this thesis, we only consider  $\frac{1}{\Gamma} > \frac{1}{\Delta_{B_0}}$  to prevent too complex beat structures.

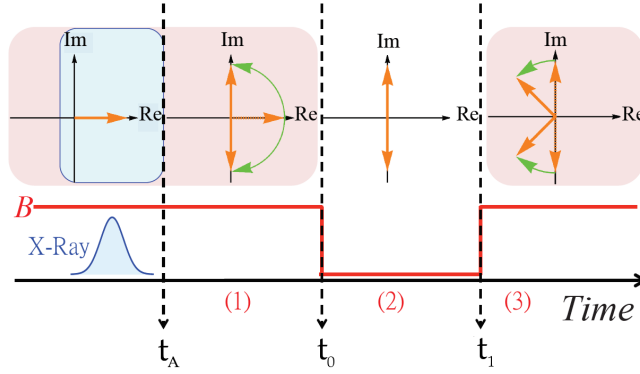


Figure 6: Visualization of the rotating current matrix elements. The x-ray reaches the target at  $t_A$ . During time interval (2), the magnetic field is switched off and the current matrix elements (see Eq. 2.41) are frozen on the imaginary axis. Image courtesy of Wen-Te Liao [23].

### 3.2 STORAGE EFFECT

The idea of storing a photon emerges from manipulating the Zeeman splitting by applying a time-dependent B-field. In particular, the switching between a vanishing and a non-vanishing B at specific times is the essence of the storage effect.

For the time we apply a non-vanishing field, we expect to observe the QB. Our results in figure 5.ii) show: at the instance of turning B to zero, the pattern switches into the Dynamical Beat. The time  $t_0$  controls the suppression of the Dynamical Beat after switching (green) versus the unperturbed one (red). Hence, the highest signal suppression is obtained by switching in a QB minimum.

Switching the magnetic field off at time  $t_0$  ceases the QB and stores the photon. By turning B back on at  $t_1$  the photon is released and we can observe the coherent storage effect: the QB continues its dynamics exactly at the point it was ceased before. As we will see in the next chapter, this storage process is repeatable and can be performed several times.

An explanation [1] for the storage effect is given by figure 6. As long the magnetic field is present, the two transition current matrix elements (Eq. (2.41)) rotate in the complex plane with  $\omega_{QB} = \Delta_B$  relative to each other. They both start parallel on the real axis, which is why they destructively superimpose on

the imaginary axis after half a period  $T_{QB}/2$  (which is the instance of a QB minimum).

If we switch off the field at this instant, the rotation freezes and the destructive interference of the currents holds for as long as the field stays off.

This scheme conserves photon energy, polarization and phase [23] of the coherently stored photons. However, we can see that storage time, just as the unperturbed signal lifetime, is still limited by incoherent natural decay processes draining energy from the system.

### 3.3 PHASE MODULATION

Rotating the magnetic field by  $\pi$  rad, i.e. inverting its value, causes the reversed time effect [1] in which the nuclear currents evolve backwards in time. This induces a shift in the photon phase of  $\pi$  rad (fig. 7), which is independent of an eventual photon storage period.

We demonstrate this phase shift effect in figure 7 by implementing an according magnetic field inversion at time  $t_s$  into the MBE (2.46). We set  $\xi = 60$  and choose the storage time to be zero.

Having demonstrated the fundamental effects of switching the B-field without an alteration of the (sign-insensitive) direction of the quantization axis, we proceed to investigating the features of more complex magnetic switching sequences in the next chapter.



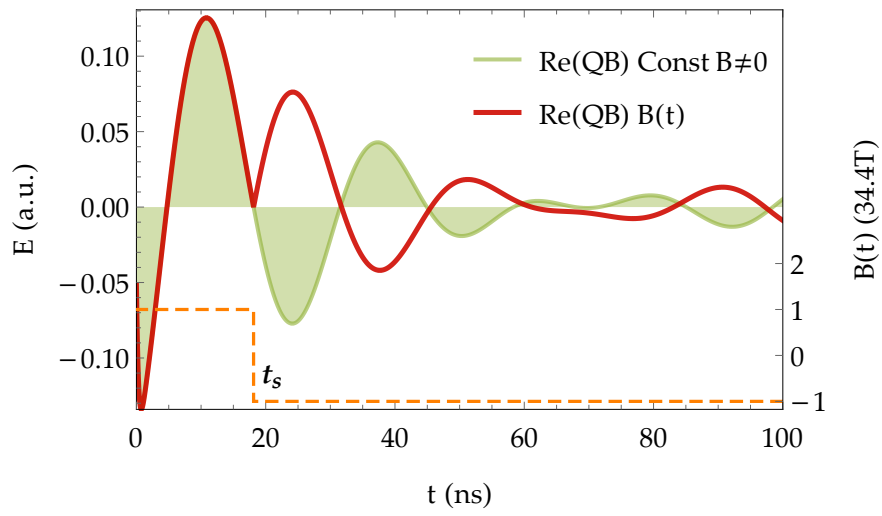


Figure 7: Time evolution of the real part of the scattered radiation at position L. The magnetic field is rotated by  $\pi$  rad at time  $t_s$ . This field inversion induces a phase shift in the electric field  $E(L, t)$  wave of  $\pi$  rad.



## GENERATION AND CONTROL OF FREQUENCY COMBS

---

This chapter is dedicated to investigating the effects of periodic magnetic switchings on the NFS spectrum. The previously introduced photon storage and phase modulation (chapter 3) are repetitively performed in periodic patterns. Not only the time, yet also the frequency spectrum is analysed. We find that the periodicity in the switching generates frequency combs with equidistant peaks in the forward scattered radiation. The combs' shape can be controlled via the periodic properties of the magnetic switching.

To document the method used for viewing the frequency domain, we initially introduce the Fourier transform utilized to switch into frequency space. For verification of the implemented transform, we compare our results for the unperturbed QB with the theoretical expectations.

Consecutively, we systematically simulate time and frequency domains under the imposition of periodic magnetic field switchings. We proceed by analysing the qualitative behaviour of the combs.

Finally, we present a semi-analytical description of the scattered spectra. We construct an integrable function that, in first order, simulates the time spectrum. This permits us to find the analytic Fourier transform qualitatively leading to the observed frequency combs.

Throughout this chapter, we set the optical thickness  $\xi$  sufficiently low to suppress multiple scattering processes for the duration of our scope. In good approximation, the QB envelope is then given by the exponential decay  $e^{-\Gamma t}$  [29]. But more importantly, the beat lopes becomes equidistant, so that it would become easier to experimentally implement a periodic switching sequence aligned with the beat.

#### 4.1 FOURIER TRANSFORM

As mentioned in the chapters before (2, 3), we obtain our forward scattered light dynamics  $\Omega(z, t)$  from numerically solving a set of PDE, the Maxwell-Bloch Equations (MBE, Eq. (2.46) on page 30). Up to this point, there is no analytic solution of these equations available. Therefore, we can only resort to the, yet very exact, numerical approximation and have to turn to a discrete Fourier transform instead of an analytic one.

Given a finite complex series  $u = (u(1), \dots, u(N))$  of  $N$  sampled function values, the transform is implemented in Wolfram Mathematica as

$$\mathcal{F}[u] =: \tilde{u}(\omega) = \frac{1}{\sqrt{N}} \sum_{t=1}^N u(t) e^{-2\pi i(t-1)(\omega-1)/N}. \quad (4.1)$$

As the indices run from 1 to  $N$ , we cannot implement negative frequencies directly.

The solution comes from assuming the input  $u$  to be an  $N$ -periodic sequence given in equidistant entries (of distance  $\Delta t$ ). The transform holds the same periodicity. Therefore, higher, next period frequencies correspond to negative frequencies:

$$\begin{aligned} \tilde{u}(\omega + N) &= \tilde{u}(\omega), \text{ so that} \\ \tilde{u}(N - 1) &= \tilde{u}(-1). \end{aligned} \quad (4.2)$$

With the zero frequency term given at the first position ( $\tilde{u}(1)$ ), we shift our data points by  $\frac{N-1}{2}$  entries to center the spectrum around zero.

By transform default, the width of the frequency range ( $f_{\text{range}}$ ) is given as an integer  $f_{\text{range}} = N$  with the equidistant steps  $\Delta f$  on the frequency scale corresponding to  $\Delta f = 1$ .

To obtain viable results, we normalize  $f_{\text{range}}$  so that it corresponds to the period  $T$  in the time spectrum,  $f_{\text{range}} \stackrel{!}{=} \frac{2\pi}{\Delta t}$ , and so that the unit steps  $\Delta f$  are meaningful:  $\Delta f = \frac{f_{\text{range}}}{N} = \frac{2\pi}{N\Delta t}$ . Now, a step in the frequency domain has a fixed translation into an actual frequency unit that is directly comparable with the time spectrum unit.

For normalization of the y-axis, we scale  $\tilde{u}$  by a factor  $\frac{T}{\sqrt{2\pi N}}$  so that it matches the continuous Fourier transform.

In figure 8.i) we simulate the time spectrum for the parameters  $\xi = 0.5$  and a

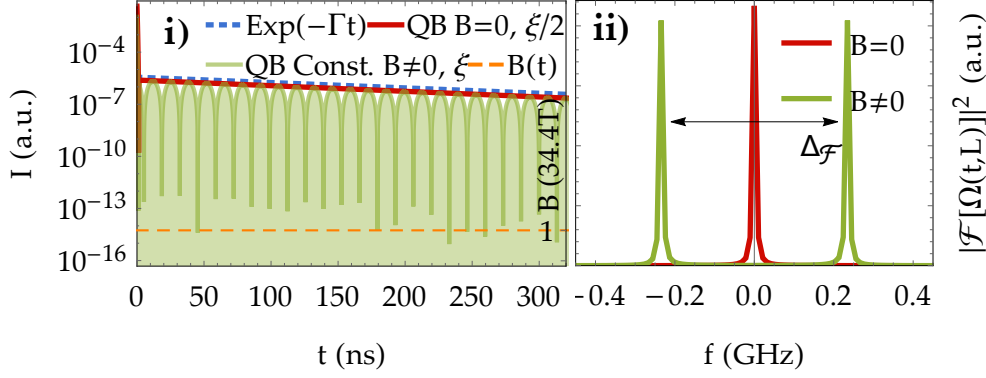


Figure 8: **i)** Time spectrum for a constant magnetic field and optical thickness  $\xi = 0.5$ . The Dynamical Beat agrees with the natural exponential decay, while the QB shows a decaying, absolute-cosine-like oscillation. **ii)** The Dynamical Beat consists of the  $\omega_0$ -frequency, the QB incorporates the two transition frequencies  $\omega_{41}$  and  $\omega_{32}$ .

constant magnetic field  $B = 34.4$  T. The MBE are numerically solved over a time range of 600 ns, which is used for all following MBE solutions as well. The length of the time range consigned to the transform determines its resolution, the larger the range the higher the resolution in the frequency spectrum. Part **ii)** of figure 8 shows the results for the Dynamical and the unperturbed Quantum Beat in the frequency domain. It is crucial to bear in mind, that we see frequencies relative to  $\omega_L \stackrel{\Delta=0}{=} \omega_0$  due to our transformation into the rotating frame (see chapter 2).

As expected, for  $B = 0$  only the principal transition frequency  $\omega_0$  occurs. With a constant magnetic field  $B \neq 0$ , we observe the frequencies of the two Zeeman-split transitions  $\omega_{41}$ ,  $\omega_{32}$ . We may verify our transform by reading out their distance  $\omega_{41} - \omega_{32} =: \Delta_{\mathcal{F}}$ .

Since the Zeeman-splitting  $\Delta_{B_0} = \Delta_g + \Delta_e$  (cf. fig. 3 on page 17) equals the QB frequency  $\omega_{QB}$ , we expect for the marked peak separation in plot **ii)**:  $\Delta_{\mathcal{F}} = \omega_{QB} = \Delta_{B_0}$ .

With  $\Delta_{\mathcal{F}} \approx 0.46915\text{GHz}$  and  $\Delta_{B_0} \approx 0.4612\text{GHz}$ , we incur a divergence of 0.006%. Considering the limited resolution, we view our transform as verified.

Note that, to easily exempt the direct response from the incident pulse itself and prompt scattering processes close to  $t = 0$  other than the resonant NFS, we only transform from the first QB minimum to the last in the time range over

which we solved the MBE. These minima are at 5 ns and 595 ns respectively in the time range shown in the plots. We presume that the key characteristics of the following observations remain when instead transforming the full spectrum with the initial light pulse cut off as it is shown in the plots. However, since that would include the signal of other scattering processes with no or different periodicity, the frequency spectra would gain noise.

## 4.2 QUALITATIVE ANALYSIS

We now proceed to simulate the spectra when the probe is immersed in periodically switched magnetic fields.

We have implemented two main kinds of switching sequences:

- a non-inverting one (NInv), alternating between the magnetic field at full strength and zero, and
- an inverting one (Inv), switching between B at full strength, zero and B at full strength rotated by  $180^\circ$ .

The critical parameters of these sequences are the time intervals of the different stages. We denote the storage time, during which the field is not present, as  $\tau_{\text{off}}$ . As seen in the preceding chapter 3, this period can be chosen without constraints.

The B-field on-time we refer to as  $\tau_{\text{on}}$ . As to our aim of achieving maximum signal suppression,  $\tau_{\text{on}}$  is restricted to multiples of  $\frac{T_{\text{QB}}}{2}$ .

### *Non-Inverting Sequence*

We implement the non-inverting sequence into the MBE and solve them for different storage times in combination with a fixed  $\tau_{\text{on}}$  of half a QB period. As before in figure 8,  $\xi$  is set to 0.5 and  $B_0$  to 34.4 T. The numerical results in figure 9 reveal: under the influence of the periodic switching, the two peaks seen before in figure 8 split into several equidistant spikes in the frequency domain. Thus, a frequency comb is formed.

To check the equidistance, we evaluated the peak positions. They are drawn as black-dotted lines into the graphs. The average peak distance has a standard deviation of 0% up to circa 5% for different combs. We attribute this deviation

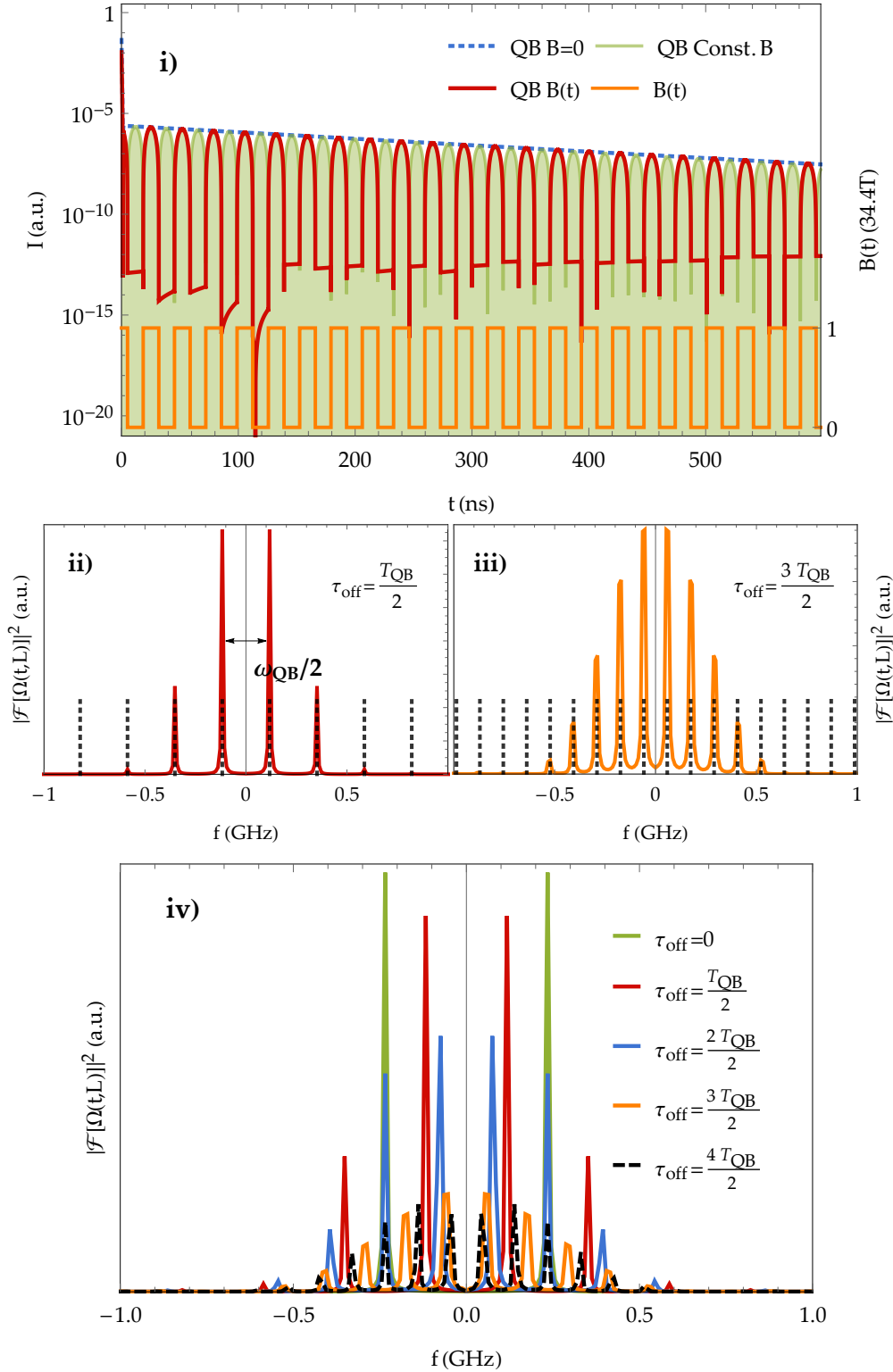


Figure 9: **i)** Time spectrum for  $\tau_{\text{on}} = \tau_{\text{off}} = \frac{T_{\text{QB}}}{2}$  (red). **ii)** and **iii)** Single frequency spectra for different  $\tau_{\text{off}}$  at fixed  $\tau_{\text{on}} = \frac{T_{\text{QB}}}{2}$ . The black dotted lines mark the equidistant peak positions. **iv)** Multiple frequency spectra for different  $\tau_{\text{off}}$  in comparison. With a growing storage time, the peaks multiply and narrow towards  $\omega_0$  while the overall intensity drops. The spectra of  $\tau_{\text{off}} = 0$  and  $\frac{T_{\text{QB}}}{2}$  have been manually downscaled by 80% and 50% respectively to allow for a proper display.

to the limited resolution and thereby limited precision of the peak positions. This is supported by the fact, that there is no systematic or biased divergence acknowledgeable.

In figure 9, the signals for varying  $\tau_{\text{off}}$  and  $\tau_{\text{on}}$  are displayed. From this and further not depicted simulations, we conclude the following:

- At constant  $\tau_{\text{on}}$ , the separation of the peaks in the frequency combs narrows with growing  $\tau_{\text{off}}$ . The peaks drift towards the origin ( $\omega_0$ ) and new peaks gain intensity at the border regions (towards  $\pm 1\text{GHz}$ ). The two frequencies  $\omega_{41}$ ,  $\omega_{32}$  appear in the combs for every  $\tau_{\text{off}}$  set to an even multiple of  $\frac{T_{\text{QB}}}{2}$ . Due to maximum signal suppression during  $\tau_{\text{off}}$ , the overall intensity declines as we increase this parameter.
- For a constant  $\tau_{\text{off}}$  but a varying  $\tau_{\text{on}}$ , we may lose the equidistant peak separation: if  $\tau_{\text{on}}$  is sufficiently large to allow only for a very few switchings, we have an almost unaltered time spectrum in comparison to the constant magnetic field. In consequence, we see almost just the two constant-field beat frequencies. But, as becomes evident for reducing  $\tau_{\text{on}}$ , the two frequency peaks at  $\omega_{41}$ ,  $\omega_{32}$  split into two spikes. Their separation grows for a declining  $\tau_{\text{on}}$ . No additional high-intensity peaks emerge. We have done simulations with  $\tau_{\text{on}}$  in a range from  $\frac{T_{\text{QB}}}{2}$  to the point at which the field is only switched once,  $\frac{45T_{\text{QB}}}{2}$ .
- We tested keeping the relation between switching times constant,  $\tau_{\text{on}} = \tau_{\text{off}} =: \tau_S$ . Increasing  $\tau_S$  produces a mixture of the previous two scenarios. The peaks are narrowing, yet not towards  $\omega_0$ , but  $\omega_{41}$  and  $\omega_{32}$ . At uneven multiples of  $\frac{T_{\text{QB}}}{2}$ , we see the two highest peaks adjacent to  $\omega_{41}$ ,  $\omega_{32}$ . At even multiples they appear exactly at those two points.

We conclude that suitable frequency combs may only be generated for  $\tau_{\text{on}} = \frac{T_{\text{QB}}}{2}$ .

### *Inverting Sequence*

This sequence differs from the NInv one in that the orientation of the B-field is inverted after every off-switching. This  $180^\circ$  rotation causes a  $\pi$ -phase shift in the time domain (see fig. 7 on page 39). As this phase shift is equivalent



to flipping every second beat lobe with respect to the time axis, the intensity time spectrum remains the same as before.

In figure 10, we present the implementation of the Inv sequence for several storage times  $\tau_{\text{off}}$  ranging from 0 to  $4T_{\text{QB}}/2$ . We give an example for the scattered field (real and imaginary part), that demonstrates the functionality of the switching sequence. Furthermore, we compare the Fourier spectra for the Inv and NInv series for two exemplary storage times and show how controlling the storage time influences the comb shape.

Interestingly, the Fourier spectra of the Inv switching differ significantly from the NInv case. The frequency combs generated with the inverting sequence all have their highest peak at  $\omega_0$ .

For varying  $\tau_{\text{off}}$  (shown in fig. 10.iv)) and fixed  $\tau_{\text{on}}$  as done for the NInv sequence above, these combs show an analogous behaviour. The  $\omega_0$ -peak vanishes for even  $n$  in  $\tau_{\text{on}} \geq \frac{nT_{\text{QB}}}{2}$ .

As we can infer from figure 10.ii), the Inv combs are shifted relative to the NInv combs by half their equidistant separation.

Another remarkable effect comes up in figure 10.iii) when setting the storage time to zero. Then, the magnetic field is constantly and immediately inverted after  $\tau_{\text{on}}$ . The phase shift results in an E-field time spectrum that resembles a flipped absolute cosine. The intensity spectrum is the same as with a constant B-field.

However, in contrast to the QB in the case of a constant field, we do not see the two transition frequencies. Instead, the frequency spectrum shows a large intensity peak at  $\omega_0$  and two smaller ones each separated by  $\Delta_{B_0}$  from the origin.

Again, the shift distance between the corresponding ( $\tau_{\text{off}} = 0$ ) NInv spectrum peaks (green in fig. 10.iii)) and the Inv is half the equidistance, in the plotted case  $\frac{\Delta_{B_0}}{2}$ .

### 4.3 ANALYTIC APPROACH

To obtain a better comprehension of the observed phenomena, we attempt a semi-analytic description of the spectra. The term semi-analytic is proposed to convey that we do not analytically solve the underlying differential equa-

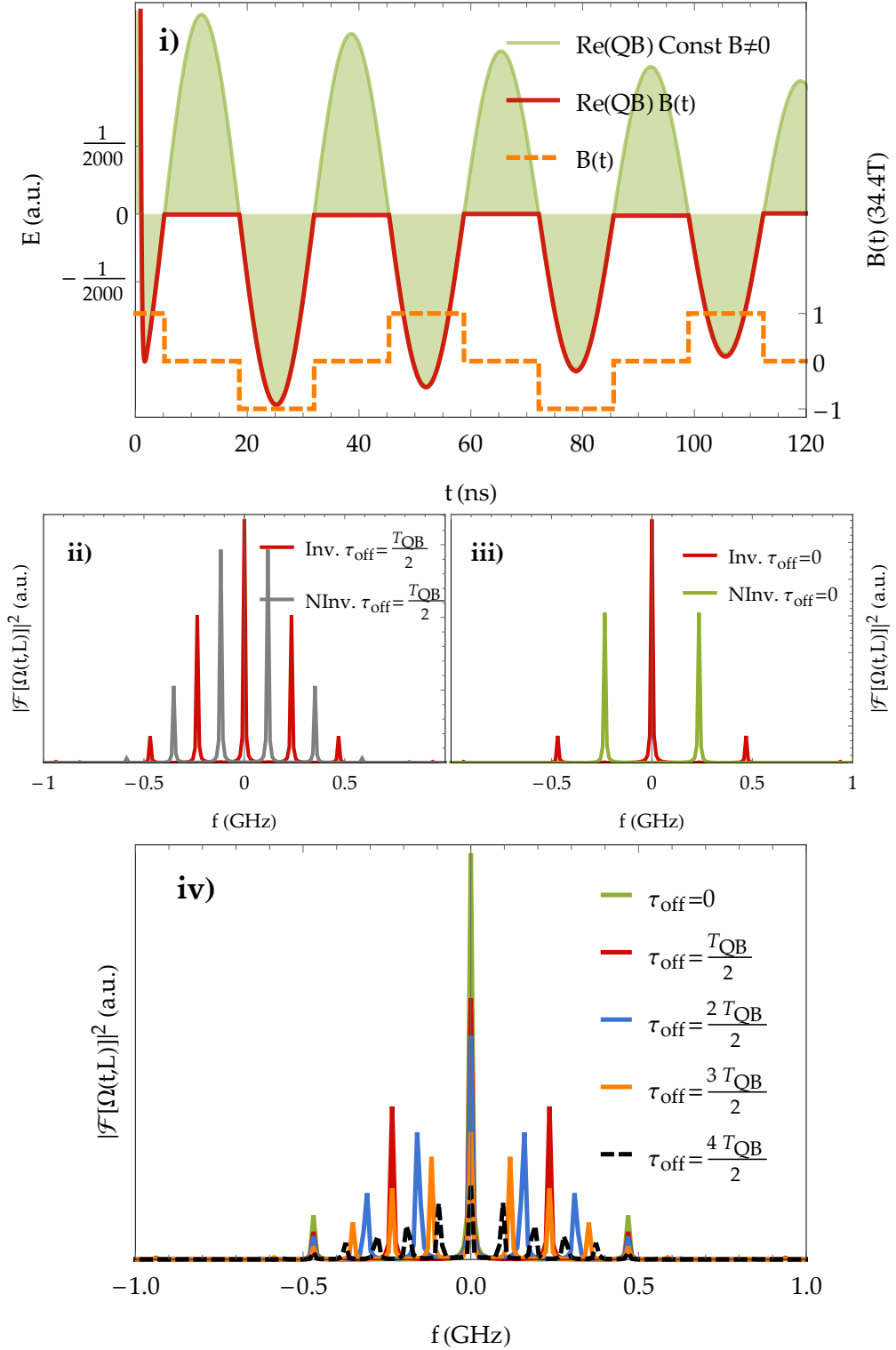


Figure 10: **i)** E-field amplitude time spectrum for the inverting sequence at  $\tau_{\text{on}} = \tau_{\text{off}}$  set to half the QB period. The field direction is inverted after every storage. **ii)** and **iii)** Frequency combs for  $\tau_{\text{off}} = \frac{T_{\text{QB}}}{2}$  and  $= 0$  respectively in comparison with the inverting and non-inverting switching. **iv)** Frequency combs of the inv. sequence for several different storage times. The spectra of  $\tau_{\text{off}} = 0$  and  $\frac{T_{\text{QB}}}{2}$  have been manually downscaled by 80% and 50% respectively to allow for a proper display.

tions ((2.46) in chapter 2), yet we find an analytic function that models the observed time spectra in first order. This function is then analytically Fourier transformed and compared to the actual, discrete transform from the preceding sections.

For a constant magnetic field, the time spectrum dynamics can be modelled by a cosine-function combined with an exponential decay term:

$$\Omega(L, t) \approx A \cdot \cos(\omega_{\text{QB}}t + \phi) e^{-\frac{\Gamma}{2}(t+t_s)} \Theta(t), \quad (4.3)$$

with a constant amplitude  $A$ , phase shift  $\phi$  and shift time  $t_s$  to correctly render the starting time of the natural decay. The Heaviside-Theta-function  $\Theta(t)$  ensures our spectrum starts at time  $t = 0$ .

We set  $\phi = \frac{-\pi}{2}$  and  $t_s$  to the time of the first QB minimum, so that the spectrum is reconstructed from the same origin we have chosen for the discrete transform in the preceding sections.

The general time spectrum for a non-vanishing storage time  $\tau_{\text{off}}$  resembles a series of single, cut-off cosine-beats:

$$\Omega_{\text{single}}(L, t) = A e^{-\frac{\Gamma}{2}t_s} \cos(\omega_0(t - t_1) + \phi) e^{-\frac{\Gamma}{2}t} \Theta(t - t_2) \Theta(t_3 - t). \quad (4.4)$$

The shifting time  $t_1$  controls the starting point of the single cosine beat lobe. The other two ( $t_2$  and  $t_3$ ) set its cut-off positions.

The full spectrum is given by the sequence of these single beats, i.e.:

$$\Omega(L, t) = \sum_{n=0}^{\infty} \Omega_{\text{single}}(L, t, n), \quad (4.5)$$

where the  $n$ -dependence is introduced in the shifting times  $t_i = t_i(n)$ ,  $i = 1, 2, 3$ . The explicit form of  $t_i(n)$  is stipulated by the switching sequence type; the inverting and non-inverting type only differ in their form of the shifting times.

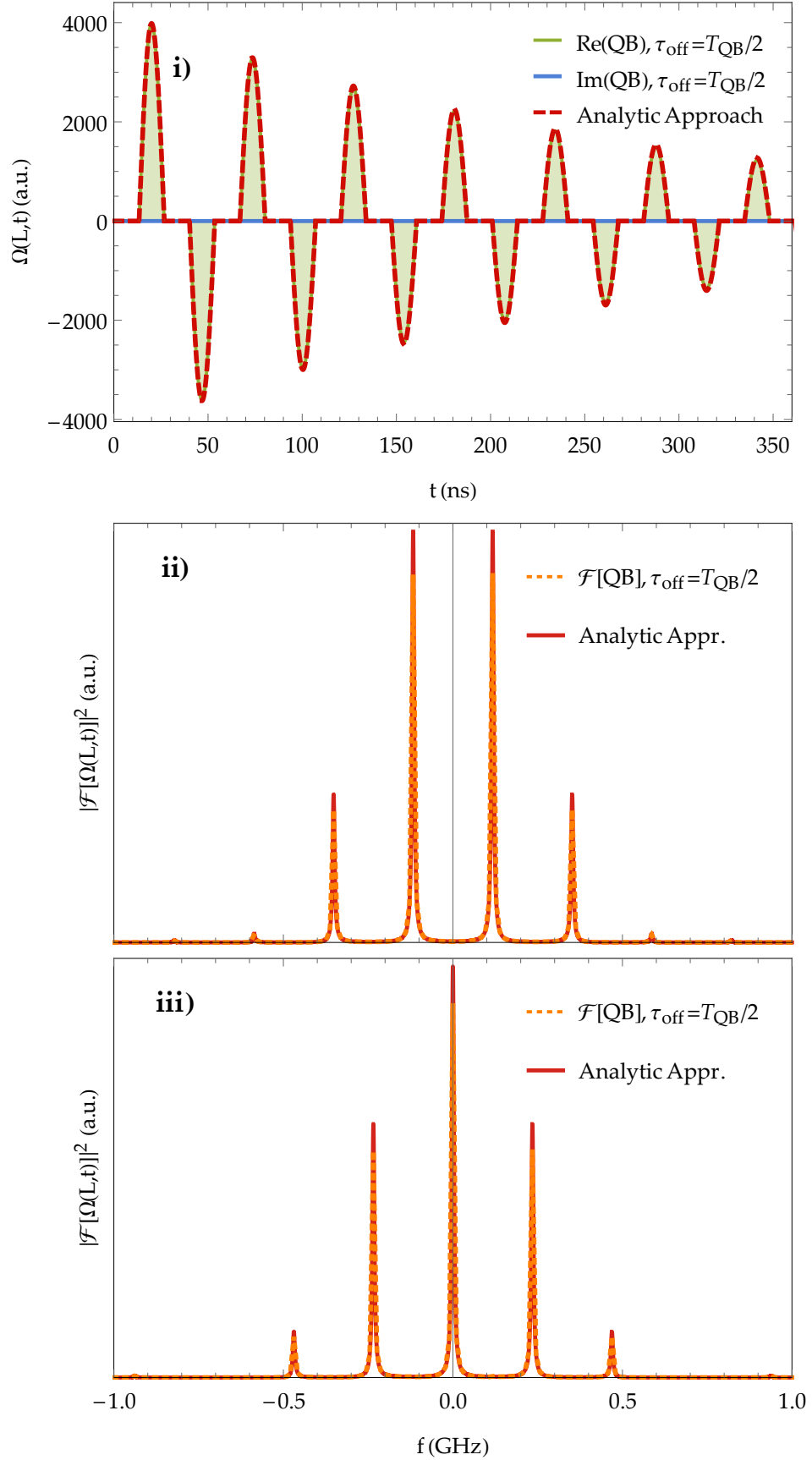


Figure 11: **i)** An example plot of the numerically solved NFS time spectrum from the MBE (green and blue) for the non-inverting sequence at  $\tau_{\text{off}} = \tau_{\text{on}} = T_{\text{QB}}/2$  in comparison with the analytic approach defined in section 4.3. The imaginary part of the scattered amplitude is zero. **ii)** and **iii)** Discrete Fourier transforms (orange dashed) compared to the analytic approach (red) for the non-inverting as well as inverting sequence, each at a storage time of half a QB period.

The Fourier transform of the single lobe is

$$\begin{aligned}
\tilde{\Omega}_{\text{single}}(L, \omega) &:= \mathcal{F}[\Omega_{\text{single}}(L, t)] \\
&= \frac{Ae^{-\frac{\Gamma}{2}t_s}}{\sqrt{2\pi}} \int_{-\infty}^{\infty} \cos(\omega_{\text{QB}}(t-t_1) + \phi) e^{-\frac{\Gamma}{2}t} \\
&\quad \times \Theta(t-t_2)\Theta(t_3-t) \cdot e^{i\omega t} dt \\
&= \frac{Ae^{-\frac{\Gamma}{2}t_s}}{\sqrt{2\pi}} \left( \frac{e^{i(\phi-\omega_{\text{QB}}t_1)}}{i(\omega_{\text{QB}}+\omega)-\frac{\Gamma}{2}} \cdot e^{t(i(\omega_{\text{QB}}+\omega)-\frac{\Gamma}{2})} \Big|_{t_2}^{t_3} \right. \\
&\quad \left. - \frac{e^{i(\omega_{\text{QB}}t_1-\phi)}}{i(\omega_{\text{QB}}-\omega)+\frac{\Gamma}{2}} \cdot e^{-t(i(\omega_{\text{QB}}-\omega)+\frac{\Gamma}{2})} \Big|_{t_2}^{t_3} \right). \tag{4.6}
\end{aligned}$$

As the Fourier transform is a linear functional, we may reduce the transform of the whole spectrum sequence (Eq. (4.5)) to a series of the single transforms:

$$\begin{aligned}
\tilde{\Omega}(L, \omega) &:= \mathcal{F}\left[\sum_{n=0}^{\infty} \Omega_{\text{single}}(L, t, n)\right] \\
&= \sum_{n=0}^{\infty} \mathcal{F}[\Omega_{\text{single}}(L, t, n)] = \sum_{n=0}^{\infty} \tilde{\Omega}_{\text{single}}(L, \omega, n). \tag{4.7}
\end{aligned}$$

Our analytic approach exploits the exponential decay form of the QB envelope for small  $\xi$ , it is therefore not valid for a larger optical thickness. It as well takes advantage of the vanishing of the imaginary part of the E-field amplitude, as it is shown in figure 11.i).

In figure 11.i) we show an example of the time spectrum modelling for the NInv sequence at a storage time of half a QB period to verify our approach. The optical thickness and time range (for the solution of the MBE, not the plot range) are chosen as in the preceding time spectrum plots (e.g. fig. 9.i)). As the plot shows, the analytic time spectrum model agrees, in first order, perfectly with the numerical solution from the MBE (Eq. (2.46)).

Plots ii) and iii) display the analytic transforms of the Inv and NInv sequences for  $\tau_{\text{off}} = \frac{T_{\text{QB}}}{2}$ . The analytic frequency spectrum is in very good agreement with the discretely transformed one from the MBE. The slightly higher intensities in the analytic transform are rooted in the limited resolution of the discrete transform. While the latter is limited to a time spectrum input of the duration for which we solved the MBE (the mentioned time range of approximately

600 ns), the former can resort to a significantly larger time span. Thereby, the analytic peaks count more beat loops that constructively contribute to their height.

#### 4.4 FEASIBILITY

Up to this point in this thesis, we have implemented the magnetic field switching as instantaneous. This approach is the simplest to theoretically investigate and understand the behaviour of time and frequency spectra of the scattered photons. But it is not realistic as an infinitely steep switching cannot be implemented in an experimental setup. Therefore, we dedicate this section to test smoothed magnetic switchings with a finite, experimentally more feasible slope.

Initially, we introduce an exponential smoothing of our rectangle pulse function, as shown in figure 12. The smoothing used is described by the following exponential function:

$$\begin{aligned} \text{smRect}(t, t_0, t_1) := & \left(1 - \frac{1}{1 + \exp\left(\frac{t-t_0}{\epsilon}\right)}\right) \Theta\left(t_0 + \frac{t_1 - t_0}{2} - t\right) \\ & + \frac{1}{1 + \exp\left(\frac{t-t_1}{\epsilon}\right)} \Theta\left(t - \left(t_0 + \frac{t_1 - t_0}{2}\right)\right), \end{aligned} \quad (4.8)$$

with smoothing radius  $\epsilon$  and  $\Theta(t)$  as the Heaviside-Theta function.

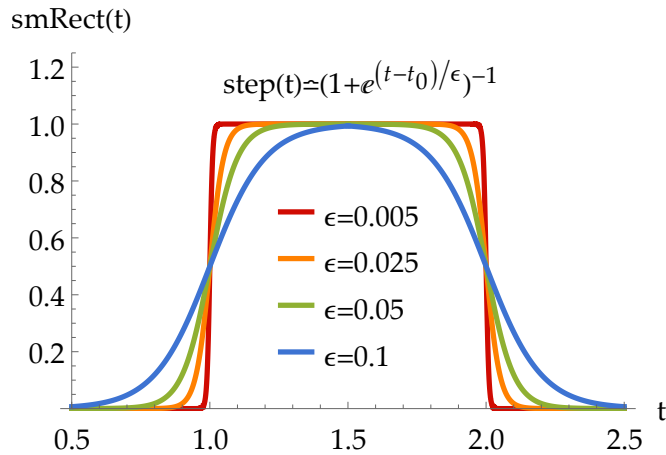


Figure 12: Exponentially smoothed rectangle pulse for step up at  $t_0 = 1$  and step down at  $t_1 = 2$ . The effect of the smoothing radius  $\epsilon$  depends on the value of those two parameters.

Finally, as an ultimate accommodation for the experimental practicability, we give up one degree of freedom by constraining B-field off- and on-time to be the same,  $\tau_{\text{off}} = \tau_{\text{on}}$ . This enables the switching sequence to be produced by a sinusoidal signal.

Our simulations with these smoothed sequences show one main result: Up to a certain, significantly large degree of smoothing, the frequency spectra stay basically unaltered with respect to the unsmoothed switching.

As a numerical example, we present figure 13. For the same  $\xi$ , as in the sections before, figure 13 shows the results of smoothing the switching for the non-inv. sequence at  $\tau_{\text{off}} = \tau_{\text{on}} = \frac{T_{\text{QB}}}{2}$ . The Fourier transform is performed over the same range as previously, from the first to the last QB minimum (now appr. at 606 ns). In part **i)** the switching sequences for different smoothings are compared, so that the degree of smoothing becomes tangible. The smoothing radius for the exponentially smoothed step (orange) was chosen as  $\epsilon = 0.5$  ns. Plot **ii)** gives an extract of the time spectrum for the differently smoothed QB. A significant deviation of the smoothed versus the abrupt switchings is visible. In part **iii)** we compare the frequency spectra of the various sequences. Except for slight intensity deviations, the main characteristics of the frequency combs are maintained. Even the sinusoidal signal, which is likely to be the simplest to experimentally implement, shows no significant frequency spectrum distortion.

Thus, we conclude that our previous findings bear the realistic opportunity of an experimental implementation.

In terms of the experimental realization, the fundamental constituent is the coherent x-ray source. However, with the advent and anticipated improvement of x-ray free electron lasers (XFEL) [25, 43, 44], another core challenge remaining is the implementation of the ultra-fast magnetic switching.

One possibility of achieving this aim could be via so called snapper capacitors [45] using few-turn coils and a moderate pulse current of approx. 15 kA from the low-inductive high-voltage capacitors [23]. Another interesting prospect is the "Lighthouse Setup" [22, 46] shown in figure 14: Instead of switching the field, the sample is rotated in and out of its reach. A small rotor, which is only a few mm in cross-section, achieves rotational frequencies  $\omega_R$  of up to 70 kHz. It is expected to be fast enough to rotate the sample out a depth of few  $\mu\text{m}$  in

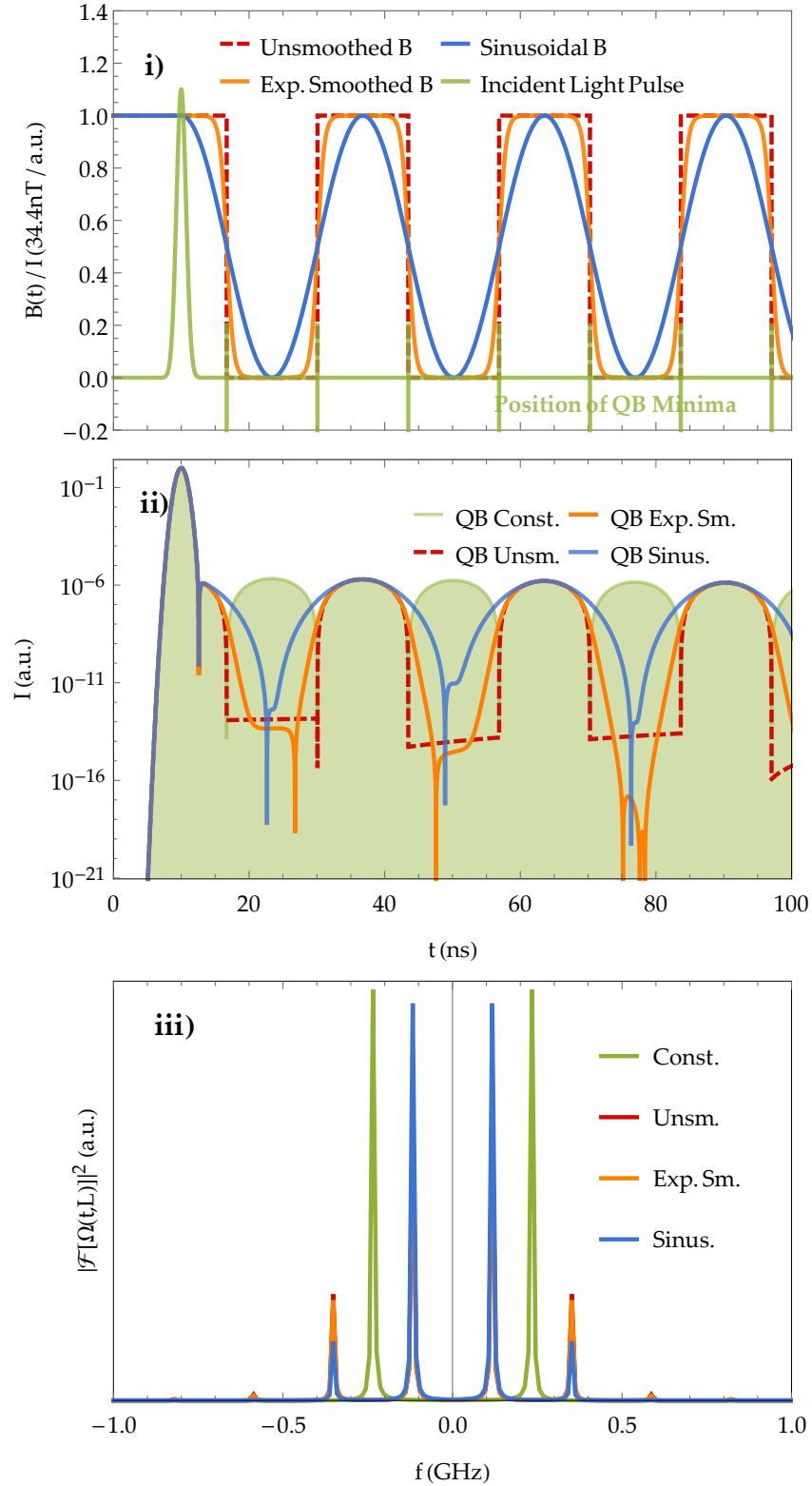


Figure 13: **i)** Abrupt and differently smoothed magnetic switching sequences for  $\tau_{\text{on}} = \tau_{\text{off}} = T_{\text{QB}}/2$  in comparison. The smoothing radius for the exponential step (orange) was set to  $\epsilon = 0.5$  ns. Different than in the previous sections, we display the time spectrum with the origin set before the light pulse arrival at  $t = 10$  ns. The Fourier transform is performed over the same range as previously, from the first to the last QB minimum ( $\approx 606$  ns). **ii)** Extract of the time spectrum for different QB. The origin is chosen the same as in the preceding B-field sequences plot. **iii)** Frequency spectra of the various sequences. Except for slight intensity deviations, the main characteristics of the frequency combs are maintained. Even the sinusoidal signal, which is likely to be the simplest to experimentally implement, shows no significant frequency spectrum distortion. The constant spectrum (green) was rescaled by 50% to fit into the display.



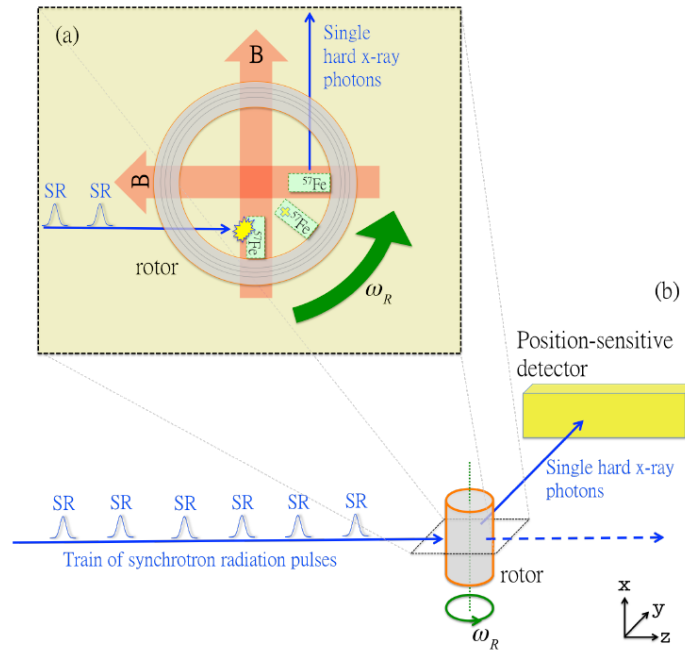


Figure 14: **a)** The Lighthouse Setup from a top view. The sample (light green rectangles) is mounted onto a small rotor. It rotates (green arrow) with frequency  $\omega_R$  in and out of two static magnetic fields  $B$  (red arrows). Meanwhile, a pulse from an x-ray source, e.g. Synchrotron Radiation (SR), impinges perpendicularly on the target. **b)** The Lighthouse Setup in side view. Image courtesy of Wen-Te Liao [23].

fractions of ns [23].



## SUMMARY AND OUTLOOK

---

In this thesis we have investigated the effects of applying periodic magnetic switching series in a Nuclear Forward Scattering (NFS) setup. We found that under the consideration of certain parameters frequency combs emerge in the forward scattered radiation. These combs offer two possible applications. First of all, as a measurement instrument in the usual sense of frequency combs. Second, since their distinctive form can be controlled via the magnetic switching, as an information carrier.

In the NFS setup we chose (see sec. 1.2 on page 6) for our theoretical investigations, only the two  $\Delta M = 0$  transitions between the ground and first excited state of  $^{57}\text{Fe}$  Mößbauer nuclei are driven by a short x-ray pulse of 1 ns duration. When the resonant x-ray penetrates the target, the excitation is delocalized and recoilless, allowing for Multiple Scattering effects in the forward re-emitted radiation. Additionally, in the presence of an external magnetic field, the two magnetic sublevel transitions interfere and produce a pattern characteristic for NFS, the Quantum Beat (QB).

Performing a single, timed off- and subsequent on-switching of the external magnetic field permeating the nuclei leads to a coherent storage of the forward scattered photon. An inversion of the magnetic field direction however causes a  $\pi$ -shift of the photon phase.

These two mechanisms of storage and phase modulation constitute the basis of our periodic switching sequences. Therefore, we verified our implementation of both (chap. 3) with previously published results [1].

Our new numerical results show: Weaving a certain periodicity into the magnetic switching generates periodicity in the frequency spectrum of the forward scattered radiation. Thereby, for adequate switching parameters, equidistant frequency combs emerge in the scattered radiation.

We applied two types of switching sequences: a non-inverting and an inverting one. In the non-inverting sequence, the magnetic field  $B$  alternates between 0 and  $B_0$ , in the inverting one between  $-B_0$ , 0 and  $B_0$  with  $B_0 = 34.4$  T. The two tuning parameters of our switchings are

- i) the downtime  $\tau_{off}$ , during which the B-field is turned off and the photon coherently stored and
- ii) the uptime  $\tau_{on}$ , during which the magnetic field is on and the normal QB of NFS proceeds.

To achieve maximum signal suppression, the off-switching has to be performed in a QB minimum, for which reason  $\tau_{on}$  is restricted to multiples of half the QB time period  $T_{QB}$ . The storage can be chosen freely and is only limited by the natural exponential decay.

As our simulations revealed, viable frequency combs are only obtained for a minimal uptime of  $\tau_{on} = T_{QB}/2$ . Furthermore, the variation of the storage time alters the shape and intensity of the frequency combs: For an increasing  $\tau_{off}$  the equidistant peaks narrow, manifold and drift towards the central transition frequency  $\omega_0 = 14.4$  keV while the overall intensity declines. The peaks of the non-inverting and the inverting sequence are shifted against each other by half their equidistant separation.

Attempting a semi-analytical approach, we found that the time spectra can be modelled by a series of cosine functions combined with the exponential decay (sec. 4.3 on page 47). The corresponding analytic Fourier transform produces a series of Lorentz-curves that is in excellent agreement with the numerically solved combs.

For our results described above, we applied abrupt switching sequences with virtually infinite slopes. To give an estimate for the experimental feasibility of our research, we tested our findings with the implementation of experimentally more realistic switching sequences. For that purpose, we smoothed the switching processes. An exponential smoothing of the up and down steps allows for longer raising and declining times of the magnetic field while not losing any of the tuning flexibility. However, giving up one degree of freedom by restraining  $\tau_{on} = \tau_{off}$  permits the implementation of a sinusoidal field. An experimental setup could be given by the Lighthouse Setup (see fig. 14).

Simulations with these more realistic switchings disclosed that even under an extreme smoothing in the form of the sinusoidal field, the characteristic frequency spectra stay mainly unaltered. Hence, an experimental implementation seems within the realm of feasibility.

For the advancement of this topic, we see the following possibilities.

To realize the very fast magnetic switchings, it is inevitable to further investigate experimental setups that would allow for repetitive field variations in the ns-range. Setups where the field is absolutely stationary, but changing relative to the sample by moving the probe are thinkable.

Another intriguing direction to explore is the use of x-ray frequency combs as information carriers. For this we would like to investigate in what fashion the combs would need to be manipulated to process information, for example in the form of logical operations as it was recently done in Ref. [20].



Part III

APPENDIX





# A

## APPENDIX A

---

### *Radiation Gauge*

In chapter 2 we used the Radiation Gauge. Let us now take a closer look at its derivation.

Given that the source of our incident radiation is virtually infinitely far from the interaction region with the sample, we may consider the fields in the free space approximation, i.e. we have no source terms in the Maxwell equations ( $\mathbf{j}_r, \rho_r = 0$ ).

In this case, the Coulomb gauge is called radiation gauge and implies  $\Phi = 0$ .

The gauge invariance reads

$$\begin{aligned}\mathbf{A} &\rightarrow \mathbf{A} + \nabla\Lambda =: \mathbf{A}', \\ \Phi &\rightarrow \Phi - \partial_t\Lambda =: \Phi',\end{aligned}\tag{A.1}$$

with an arbitrary function  $\Lambda(\mathbf{r}, t)$ .

Suppose we have  $\mathbf{A}, \Phi$  given in the Lorentz gauge

$$\operatorname{div}\mathbf{A} = -\frac{1}{c^2}\partial_t\Phi.\tag{A.2}$$

Now, we transform as shown in Eq. (A.1) and demand  $\operatorname{div}\mathbf{A}' \stackrel{!}{=} 0$  (Coulomb gauge). This demand is fulfilled by setting  $\operatorname{div}\mathbf{A} = -\Delta\Lambda$ .

Since the gauge cannot change the physical quantities associated with the potentials, which are the observables  $\mathbf{E}$  and  $\mathbf{B}$ , the Maxwell equations have to hold for both potentials:  $\square\Phi' = 4\pi\rho_r = \square\Phi$ , which implies

$$\begin{aligned}
\Delta\Phi' &\stackrel{(A.1)}{=} \Delta(\Phi - \partial_t\Lambda) = \Delta\Phi - \partial_t(\Delta\Lambda) \\
&= \Delta\Phi + \partial_t\operatorname{div}\mathbf{A} \stackrel{(A.2)}{=} \underbrace{\left(\Delta - \frac{1}{c^2}\partial_t^2\right)\Phi}_{=-\square} = -4\pi\rho_r = 0, \tag{A.3}
\end{aligned}$$

which would make the choice of  $\Phi'(\mathbf{r}, t) = \Phi'(t)$  constant over space valid. From this we may infer:

$$\begin{aligned}
0 = 4\pi\rho_r = \square\Phi' &= \frac{1}{c^2}\partial_t^2\Phi'(t) - \overbrace{\Delta\Phi'(t)}^{=0} \\
&\iff \partial_t^2\Phi'(t) = 0. \tag{A.4}
\end{aligned}$$

Thus, we can choose  $\Phi'(t) = \Phi'$  as constant over time as well, making it a constant in total and the choice

$$\Phi' = 0$$

valid.

This leaves for the interaction Hamiltonian:

$$\hat{H}_1 = -\frac{1}{c}\hat{\mathbf{j}}(\mathbf{r}, t)\mathbf{A}(\mathbf{r}, t). \tag{A.5}$$

## BIBLIOGRAPHY

---

- [1] Wen-Te Liao, Adriana Pálffy, and Christoph H. Keitel. „Coherent Storage and Phase Modulation of Single Hard-X-Ray Photons Using Nuclear Excitons.“ In: *Physical Review Letters* 109 (2012), p. 197403.
- [2] Alberto Politi, Martin J. Cryan, John G. Rarity, Siyuan Yu, and Jeremy L. O’Brien. „Silica-on-Silicon Waveguide Quantum Circuits.“ In: *Science* 320 (2008), p. 646.
- [3] Brian Julsgaard, Jacob Sherson, J Ignacio Cirac, Jaromír Fiurášek, and Eugene S Polzik. „Experimental demonstration of quantum memory for light.“ In: *Nature* 432.7016 (2004), pp. 482–486.
- [4] Mahdi Hosseini, Ben M Sparkes, Gabriel Hétet, Jevon J Longdell, Ping Koy Lam, and Ben C Buchler. „Coherent optical pulse sequencer for quantum applications.“ In: *Nature* 461 (2009), p. 241.
- [5] G.E. Moore. „Cramming More Components Onto Integrated Circuits.“ In: *Proc. IEEE* 86 (1998), p. 82.
- [6] Bernhard W. Adams et al. „X-ray quantum optics.“ In: *J. Mod. Opt.* 60 (2013), p. 2.
- [7] P. Emma et al. „First lasing and operation of an angstrom-wavelength free-electron laser.“ In: *Nature Photon* 4 (2010), p. 641.
- [8] T. Ishikawa et al. „A compact X-ray free-electron laser emitting in the sub-angstrom region.“ In: *Nature Photon* 6 (2012), p. 540.
- [9] Y. V. Shvyd’ko, S. Stoupin, V. Blank, and S. Terentyev. „Near-100% Bragg reflectivity of X-rays.“ In: *Nature Photon* 5 (2011), p. 539.
- [10] Y.V. Shvyd’ko. *X-ray Optics: High-energy-resolution Applications*. Vol. 98. Springer-Verlag, 2013.
- [11] L. Young et al. „Femtosecond electronic response of atoms to ultra-intense X-rays.“ In: *Nature* 466.7302 (July 2010), pp. 56–61.

- [12] Ralf Röhlsberger, Hans-Christian Wille, Kai Schlage, and Balaram Sahoo. „Electromagnetically induced transparency with resonant nuclei in a cavity.“ In: *Nature* 482.7384 (2012), pp. 199–203.
- [13] T. J. Bürvenich, J. Evers, and C. H. Keitel. „Nuclear Quantum Optics with X-Ray Laser Pulses.“ In: *Phys. Rev. Lett.* 96 (2006), p. 142501.
- [14] K. Tamasaku and T. Ishikawa. „Interference between Compton Scattering and X-Ray Parametric Down-Conversion.“ In: *Phys. Rev. Lett.* 98 (2007), p. 244801.
- [15] K. Tamasaku, K. Sawada, E. Nishibori, and T. Ishikawa. „Visualizing the local optical response to extreme-ultraviolet radiation with a resolution of  $\lambda/380$ .“ In: *Nature Phys.* 7 (2011), p. 705.
- [16] Ralf Röhlsberger, Kai Schlage, Balaram Sahoo, Sebastien Couet, and Rudolf Ruffer. „Collective lamb shift in single-photon superradiance.“ In: *Science* 328.5983 (2010), pp. 1248–1251.
- [17] Kilian P Heeg, Hans-Christian Wille, Kai Schlage, Tatyana Guryeva, Daniel Schumacher, Ingo Uschmann, Kai S Schulze, Berit Marx, Tino Kämpfer, Gerhard G Paulus, et al. „Vacuum-assisted generation and control of atomic coherences at x-ray energies.“ In: *Phys. Rev. Lett.* 111.7 (2013), p. 073601.
- [18] Y. V. Shvyd'ko et al. „Storage of nuclear excitation energy through magnetic switching.“ In: *Phys. Rev. Lett.* 77 (1996), p. 3232.
- [19] J. Hannon and G. Trammell. „Coherent  $\gamma$ -ray optics.“ In: *Hyperfine Interactions* 123-124 (1999), p. 127.
- [20] J. Gunst, C.H. Keitel, and A. Pálffy. „Logical operations with single x-ray photons via dynamically-controlled nuclear resonances.“ In: *Scientific Reports* 6.25136 (2016).
- [21] Xiangjin Kong and Adriana Pálffy. „Stopping Narrow-Band X-Ray Pulses in Nuclear Media.“ In: *Phys. Review Letters* 116.197402 (2016).
- [22] R. Röhlsberger. *Nuclear Condensed Matter Physics with Synchrotron Radiation: Basic Principles, Methodology and Applications*. Berlin, Germany: Springer-Verlag, 2004.
- [23] Wen-Te Liao. *Doctoral Thesis: Coherent Control of Nuclei and X-Rays*. Heidelberg, Germany: University of Heidelberg, 2013.

- [24] S.L. Ruby. „Mössbauer experiments without conventional sources.“ In: *Journal de Physique Colloque C6 35* (1974), pp. C6–209.
- [25] J. Feldhaus, E. Saldin, J. Schneider, E. Schneidmiller, and M. Yurkov. „Possible application of x-ray optical elements for reducing the spectral bandwidth of an x-ray sase fel.“ In: *Optics Communications 140* (1997), p. 341.
- [26] A. Pálffy and J. Evers. „Coherent control of nuclear forward scattering.“ In: *Journal of Modern Optics 57* (2010), pp. 1993–2003.
- [27] Jonas Gunst. *Doctoral Thesis: Mutual control of x-rays and nuclear transitions*. Heidelberg, Germany: University of Heidelberg, 2015.
- [28] Y. V. Shvyd'ko, S. L. Popov, and G. V. Smirnov. „Coherent re-emission of gamma -quanta in the forward direction after a stepwise change of the energy of nuclear excitation.“ In: *Journal of Physics: Condensed Matter 5* (1993), p. 1557.
- [29] Yuri V. Shvyd'ko. „Nuclear resonant forward scattering of x rays: Time and space picture.“ In: *Phys. Rev. Letters B 59.14* (1998), pp. 9132–9143.
- [30] Yuri V. Shvyd'ko. „Perturbed nuclear scattering of synchrotron radiation.“ In: *Hyperfine Interactions 90* (1994), pp. 287–299.
- [31] A.R. Edmonds. *Angular Momentum in Quantum Mechanics*. 2nd ed. Princeton, USA: Princeton University Press, 1994.
- [32] M. D. Crisp. „Propagation of small-area pulses of coherent light through a resonant medium.“ In: *Phys. Rev. A 1* (1970), p. 1604.
- [33] Y. V. Shvyd'ko, U. van Bürck, W. Potzel, P. Schindermann, E. Gerdau, O. Leupold, J. Metge, H. D. Rüter, and G. V. Smirnov. „Hybrid beat in nuclear forward scattering of synchrotron radiation.“ In: *Phys. Rev. B 57* (1998), p. 3552.
- [34] U. van Bürck. „Coherent pulse propagation through resonant media.“ In: *Hyperfine Interactions 123/124* (1999), p. 483.
- [35] M. Bartelmann, B. Feuerbacher, T. Krüger, D. Lüst, A. Rebhan, and A. Wipf. *Theoretische Physik*. Heidelberg: Springer Verlag Berlin, 2015.
- [36] German J. de Valcarcel, Eugenio Roldan, and F. Prati. „Semiclassical Theory of Amplification and Lasing.“ In: *Revista Mexicana de Fisica E 52* (2006), pp. 198–214.

- [37] A. Pálffy, J. Evers, and C. H. Keitel. „Electric dipole-forbidden nuclear transitions driven by super-intense laser fields.“ In: *Phys.Rev.C77* 044602 (2008).
- [38] P. Ring and P. Schuck. *The Nuclear Many-Body Problem*. New York, USA: Springer Verlag, 1980.
- [39] M.E. Rose. *Multipole Fields*. New York, USA: Wiley, 1955.
- [40] Xiangjin Kong, Wen-Te Liao, and Adriana Pálffy. „Field control of single x-ray photons in nuclear forward scattering.“ In: *New J. Phys.*16 013049 (2014).
- [41] Marlan O. Scully and M. Suhail Zubairy. *Quantum Optics*. 6th ed. Cambridge, UK: Cambridge Universtiy Press, 2008.
- [42] Yuri V. Shvyd'ko. „Coherent nuclear resonant scattering of X-rays: Time and space picture.“ In: *Hyperfine Interactions* 123.2 (1999), pp. 275–299.
- [43] E. Saldin, E. Schneidmiller, Y. Shvyd'ko, and M. Yurkov. „X-ray fel with a mev bandwidth.“ In: *Nuclear Instruments and Methods in Physics Research Section A: Accelerators, Spectrometers, Detectors and Associated Equipment* 475 (2001), p. 357.
- [44] M. Yabashi and T. Ishikawa. *XFEL-SPring-8 Beamline Technical Design Report Ver. 2.0*. RIKEN-JASRI XFEL Project Head Office, 2010.
- [45] N. Miura, T. Osada, and S. Takeyama. „Research in Super-High Pulsed Magnetic Fields at the Megagauss Laboratory of the University of Tokyo.“ In: *Journal of Low Temperature Physics* 133 (2003), p. 139.
- [46] R. Röhlsberger, T. S. Toellner, W. Sturhahn, K. W. Quast, E. E. Alp, A. Bernhard, E. Burkel, O. Leupold, and E. Gerdau. „Coherent resonant x-ray scattering from a rotating medium.“ In: *Phys. Rev. Lett.* 84 (2000), p. 1007.

## LIST OF FIGURES

---

Figure 1	Schematic sketch of the Nuclear Exciton generation. A resonant light pulse (green) impinges on a crystal target (blue). The resulting excitation is delocalized and can therefore be described as a superposition of all possible single excitations (red). . . . .	7
Figure 2	This figure shows the Nuclear Forward Scattering setup. The x-ray (orange) propagating along the z-direction penetrates the Mößbauer target. The probe experiences a magnetic field B, that can be switched off, on and rotated by $\pi$ rad, so that the quantization axis is inverted. The inset shows the level scheme of the ground g and first excited e state of the $^{57}\text{Fe}$ sample including magnetic degeneration. The two states have the nuclear spins $I_g = 1/2$ , $I_e = -1/2$ , with magnetic quantum number degeneracies $M_g \in \{-1/2, 1/2\}$ and $M_e \in \{-3/2, -1/2, 1/2, 3/2\}$ as shown in the inset. Many thanks to Jonas Gunst [27] for providing the image basis. . . . .	9
Figure 3	Schematic depiction of the four-level system in our ansatz. The ground $ g\rangle$ and first excited state $ e\rangle$ of $^{57}\text{Fe}$ originally have six (degenerate) energy levels. The respective Zeeman splittings are denoted by $\Delta g$ and $\Delta e$ . Under the constraint of linearly polarized light in a certain B-field geometry, only the two $\Delta M = 0$ transitions with $M = \pm\frac{1}{2}$ are driven. The transition energy from the excited to the ground state is $\omega_0 = 14.4$ keV. . . . .	17
Figure 4	Schematic depiction of the decay processes in the four-level system of our ansatz. The excited state populations $\rho_{44}$ , $\rho_{33}$ decay into the ground states. . . . .	28

- Figure 5 **i)** Quantum beat of the  $\Delta M = 0$  transitions (green line) for a constant magnetic field  $B = 34.4$  T and optical thickness  $\xi = 60$ . The corresponding envelope (red line) is given by the Dynamical Beat calculated for  $B = 0$  and  $\xi = 30$ . See text for further explanations. **ii)** Coherent storage effect between  $t_0$  and  $t_1$ , the storage time can be arbitrary chosen and was set to  $\tau_{\text{off}} = 240\text{ns}$ . In both plots we used an optical thickness of  $\xi = 60$  and  $\xi/2 = 30$  respectively. . . . . 35
- Figure 6 Visualization of the rotating current matrix elements. The x-ray reaches the target at  $t_A$ . During time interval (2), the magnetic field is switched off and the current matrix elements (see Eq. 2.41) are frozen on the imaginary axis. Image courtesy of Wen-Te Liao [23]. . . . . 37
- Figure 7 Time evolution of the real part of the scattered radiation at position  $L$ . The magnetic field is rotated by  $\pi$  rad at time  $t_s$ . This field inversion induces a phase shift in the electric field  $E(L, t)$  wave of  $\pi$  rad. . . . . 39
- Figure 8 **i)** Time spectrum for a constant magnetic field and optical thickness  $\xi = 0.5$ . The Dynamical Beat agrees with the natural exponential decay, while the QB shows a decaying, absolute-cosine-like oscillation. **ii)** The Dynamical Beat consists of the  $\omega_0$ -frequency, the QB incorporates the two transition frequencies  $\omega_{41}$  and  $\omega_{32}$ . . . . . 43
- Figure 9 **i)** Time spectrum for  $\tau_{\text{on}} = \tau_{\text{off}} = \frac{T_{\text{QB}}}{2}$  (red). **ii)** and **iii)** Single frequency spectra for different  $\tau_{\text{off}}$  at fixed  $\tau_{\text{on}} = \frac{T_{\text{QB}}}{2}$ . The black dotted lines mark the equidistant peak positions. **iv)** Multiple frequency spectra for different  $\tau_{\text{off}}$  in comparison. With a growing storage time, the peaks multiply and narrow towards  $\omega_0$  while the overall intensity drops. The spectra of  $\tau_{\text{off}} = 0$  and  $\frac{T_{\text{QB}}}{2}$  have been manually downscaled by 80% and 50% respectively to allow for a proper display. . . . . 45



- Figure 10 **i)** E-field amplitude time spectrum for the inverting sequence at  $\tau_{\text{on}} = \tau_{\text{off}}$  set to half the QB period. The field direction is inverted after every storage. **ii) and iii)** Frequency combs for  $\tau_{\text{off}} = \frac{T_{\text{QB}}}{2}$  and  $= 0$  respectively in comparison with the inverting and non-inverting switching. **iv)** Frequency combs of the inv. sequence for several different storage times. The spectra of  $\tau_{\text{off}} = 0$  and  $\frac{T_{\text{QB}}}{2}$  have been manually downscaled by 80% and 50% respectively to allow for a proper display. . . . . 48
- Figure 11 **i)** An example plot of the numerically solved NFS time spectrum from the MBE (green and blue) for the non-inverting sequence at  $\tau_{\text{off}} = \tau_{\text{on}} = T_{\text{QB}}/2$  in comparison with the analytic approach defined in section 4.3. The imaginary part of the scattered amplitude is zero. **ii) and iii)** Discrete Fourier transforms (orange dashed) compared to the analytic approach (red) for the non-inverting as well as inverting sequence, each at a storage time of half a QB period. . . . . 50
- Figure 12 Exponentially smoothed rectangle pulse for step up at  $t_0 = 1$  and step down at  $t_1 = 2$ . The effect of the smoothing radius  $\epsilon$  depends on the value of those two parameters. . . . . 52

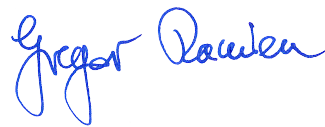
- Figure 13
- i)** Abrupt and differently smoothed magnetic switching sequences for  $\tau_{\text{on}} = \tau_{\text{off}} = T_{\text{QB}}/2$  in comparison. The smoothing radius for the exponential step (orange) was set to  $\epsilon = 0.5$  ns. Different than in the previous sections, we display the time spectrum with the origin set before the light pulse arrival at  $t = 10$  ns. The Fourier transform is performed over the same range as previously, from the first to the last QB minimum ( $\approx 606$  ns).
- ii)** Extract of the time spectrum for different QB. The origin is chosen the same as in the preceding B-field sequences plot.
- iii)** Frequency spectra of the various sequences. Except for slight intensity deviations, the main characteristics of the frequency combs are maintained. Even the sinusoidal signal, which is likely to be the simplest to experimentally implement, shows no significant frequency spectrum distortion. The constant spectrum (green) was rescaled by 50% to fit into the display. . . . . 54
- Figure 14
- a)** The Lighthouse Setup from a top view. The sample (light green rectangles) is mounted onto a small rotor. It rotates (green arrow) with frequency  $\omega_{\text{R}}$  in and out of two static magnetic fields  $B$  (red arrows). Meanwhile, a pulse from an x-ray source, e.g. Synchrotron Radiation (SR), impinges perpendicularly on the target.
- b)** The Lighthouse Setup in side view. Image courtesy of Wen-Te Liao [23]. . . . . 55

## DECLARATION

---

I insure that I have developed and written this thesis by myself and that I have not used any means or sources other than those indicated herein.

*Heidelberg, January 2017*



---

Gregor Nicolas Ramien